



저작자표시-비영리-변경금지 2.0 대한민국

이용자는 아래의 조건을 따르는 경우에 한하여 자유롭게

- 이 저작물을 복제, 배포, 전송, 전시, 공연 및 방송할 수 있습니다.

다음과 같은 조건을 따라야 합니다:



저작자표시. 귀하는 원저작자를 표시하여야 합니다.



비영리. 귀하는 이 저작물을 영리 목적으로 이용할 수 없습니다.



변경금지. 귀하는 이 저작물을 개작, 변형 또는 가공할 수 없습니다.

- 귀하는, 이 저작물의 재이용이나 배포의 경우, 이 저작물에 적용된 이용허락조건을 명확하게 나타내어야 합니다.
- 저작권자로부터 별도의 허가를 받으면 이러한 조건들은 적용되지 않습니다.

저작권법에 따른 이용자의 권리는 위의 내용에 의하여 영향을 받지 않습니다.

이것은 [이용허락규약\(Legal Code\)](#)을 이해하기 쉽게 요약한 것입니다.

[Disclaimer](#)

Master of Science

**A STUDY OF AN AIR-SPRING VIBRATION ISOLATOR
BASED ON NEGATIVE STIFFNESS STRUCTURE FOR
VEHICLE SEATS**

**The Graduate School
of the University of Ulsan
School of Mechanical Engineering
CONG HUNG NGUYEN**

**A STUDY OF AN AIR-SPRING VIBRATION ISOLATOR
BASED ON NEGATIVE STIFFNESS STRUCTURE FOR
VEHICLE SEATS**

Supervisor: Professor KYOUNG KWAN AHN

A Dissertation

Submitted to
the Graduate School of the University of Ulsan
In Partial Fulfillment of the Requirement
for the Degree of

MASTER OF SCIENCE
(Mechanical and Automotive Engineering)

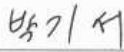
by

CONG HUNG NGUYEN

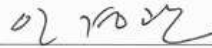
School of Mechanical Engineering
University of Ulsan, Korea
MAY 26, 2022

**A STUDY OF AN AIR-SPRING VIBRATION
ISOLATOR BASED ON NEGATIVE STIFFNESS
STRUCTURE FOR VEHICLE SEATS**

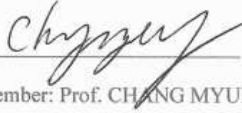
This certifies that the dissertation of
NGUYEN CONG HUNG is approved by



Committee Chair: Assistant Prof. GI-SEO, PARK



Committee member: Prof. KYOUNG KWAN AHN



Committee member: Prof. CHANG MYUNG, LEE

Department of Mechanical and Automotive Engineering

University of Ulsan, Korea

May 2022

2022

Acknowledgments

First, I would like to express my sincere appreciation and gratitude to my advisor, Professor Kyoung Kwan Ahn for the study opportunity, his support and encouragement throughout my study at the University of Ulsan.

I would like to thank Professors in the committee, Prof. Chang Myung, Lee, and Prof. Gi-Seo, Park for their suggestions and comments throughout the research.

I would express my appreciation to my colleagues in the FPMI lab, Dr. Hoai Vu Anh Truong, Ms. Tri Cuong Do, Ms. Cong Minh Ho, Ms. Manh Hung Nguyen, Ms. Hoai An Trinh, Ms. Van Du Phan, Ms. Duy Linh Vu, Mr Chau Duy Le, Mr Quang Tan Nguyen, Mr Hoang Vu Dao, Mr Thanh Ha Le, Mr Quoc Hung Hoang for their helpful discussions, great supports, inspirations and precious friendship.

Importantly, my appreciation goes towards my parents who always provide support and encouragement for me. I truly appreciate my brother and sister for their countless support.

Ulsan, Korea, May 2022

Cong Hung Nguyen

Contents

Acknowledgments.....	i
Contents	ii
List of Figures	iv
List of Tables.....	vi
Abbreviations	vii
Abstract	viii
Chapter 1 INTRODUCTION.....	1
1.1 Background	1
1.2 Research objectives.....	5
1.3 Contents of research.....	5
Chapter 2 DESIGN MODEL	6
2.1 Advantage of the air spring.....	6
2.2 The characteristics of the air spring	7
2.2.1 Sleeve air spring.....	7
2.2.2 Convolute air spring.....	10
2.3 Model description.....	11
2.4 Conclusions	13
Chapter 3 Analysis of ASVIS	14
3.1 Static analysis.....	14
3.2 Dynamic analysis	18
3.3 Conclusions.....	22
Chapter 4 SIMULATIONS RESULTS.....	23
4.1 Numerical simulation.....	23
4.2 Responses and isolation performance	25
4.2.1 Simulation setup.....	25

4.2.2 ASVIS under Sinusoidal Excitation.....	29
4.2.3 ASVIS under Multi-Frequency Wave Excitation	31
4.2.4 ASVIS under Random Excitation	33
4.3 Conclusions	36
Chapter 5 CONTROL SYSTEM MODEL	37
5.1 Sliding model control.....	37
5.2 Simulation results with SMC	40
5.3 Conclusions.....	42
Chapter 6 CONCLUSION AND FUTURE WORK.....	43
6.1 Summary	43
6.2 Future work.....	44
References	45
Publications	48
Appendix	49
I. Technical data of Sleeve Air Spring.....	49
II. Technical data of Double Convolute Bellows.....	50

List of Figures

Figure 1.1. Whole body vibration of the driver.....	1
Figure 1.2. A traditional linear isolator and its component parts.....	2
Figure 1.3. Negative stiffness structure of vehicle seat.....	3
Figure 1.4. NSS with cam-roller-spring.....	4
Figure 2.1 Types of air springs [33].....	6
Figure 2.2. Reversible sleeve and convoluted air spring [33].....	6
Figure 2.3. The analytical model of sleeve air spring.....	7
Figure 2.4. The analytical model of convoluted air spring.....	10
Figure 2.5. The general structure of the ASVIS model.....	11
Figure 2.6. Schematic diagram of ASVIS at the static equilibration position.....	12
Figure 3.1. Schematic diagram of the NSS and the crisscross structure.....	14
Figure 4.1. Non-dimensional force and non-dimensional stiffness of the NSS with $\hat{L}_h = \sqrt{2}$ and $\hat{b} = 1$. (a) Non-dimensional force; (b) Non-dimensional stiffness.....	23
Figure 4.2. Non-dimensional stiffness of the NSS for different \hat{L}_h and \hat{b} with $\alpha = 45^\circ$. (a) Non-dimensional stiffness for different \hat{L}_h ; (b) non-dimensional stiffness for different \hat{b}	24
Figure 4.3. Non-dimensional force and non-dimensional stiffness of the ASVIS with NSS. (a) Non-dimensional force; (b) non-dimensional stiffness.....	24
Figure 4.4. The effective area of the double-convoluted bellows.....	26
Figure 4.5. The volume of the double-convoluted bellows at the pressure 7 bar.....	26
Figure 4.6. The effective area of the sleeve air spring.....	27
Figure 4.7. The volume of the sleeve air spring at pressure 7 bar.....	27
Figure 4.8. Structure of the simulation model for the proposed isolators.....	28
Figure 4.9. Displacement responses of ASVIS for input frequency 3 Hz.....	29
Figure 4.10. RMS value of the displacement.....	29
Figure 4.11. Displacement responses of ASVIS for input frequency 1 Hz.....	30
Figure 4.12. RMS value of the displacement for the exaction frequency 1Hz.....	30
Figure 4.13. Displacement responses of ASVIS under multi-frequency wave excitation.....	31
Figure 4.14. RMS value of the displacement.....	31
Figure 4.15. Frequency response curves of the ASVIS.....	32

Figure 4.16. Classification of roads35
Figure 4.17. Time history results of ASVIS for random excitation..... 36
Figure 4.18. RMS value of the displacement36
Figure 5.1. Block diagram of sliding mode control38
Figure 5.2. Block diagram of the SMC in the Simulink environment.40
Figure 5.3. Response of the displacement.....41
Figure 5.4. Control signal.....41
Figure 5.5. Tracking error42

List of Tables

Table 4.1. Parameter of the sleeve-type air spring and bellows-type air spring.	28
Table 4.2. Dimension parameters of the proposed system in the simulation.	28
Table 4.3. The PSD of the road classification according to the ISO 8608.....	33
Table 4.4. The simulation parameters of the random road profile	35

Abbreviations

ASVIS	:	Vibration Isolator System with Air-Spring
NSS	:	Negative Stiffness Structure
QZS	:	Quasi-Zero-Stiffness
SLS	:	Scissor-Like Structure
PSD	:	Power Spectral Density
HB	:	Harmonic Balance Method
RMS	:	The Root Mean Square
SMC	:	Sliding Mode Control

Abstract

According to vibration theory, classical passive vibration isolators have effect in the frequency region that is higher than $\sqrt{2}$ times the natural frequency of the system. For input frequencies below $\sqrt{2}$ times the natural frequency and especially those close to the natural frequency, the vibration level of the classical isolator is really increased in comparison to the vibration level of the system. In order to overcome this issue, a novel vibration isolator system with air-spring (ASVIS) is designed for improving vibration isolation performance of the drive seat under low excitation frequencies. The main feature of the proposed system consists of two symmetric double convolution bellows which are designed by a negative stiffness structure (NSS). In addition, instead of using a vertical mechanical spring, a sleeve air spring is employed to provide positive stiffness. Moreover, a crisscross structure with two straight bars is also used as the supporting legs to provide the nonlinear characteristics with NSS.

In this research, the effects of the dimension parameters on the nonlinear force and nonlinear stiffness of ASVIS are analyzed. A design process for ASVIS is provided based on the analytical results in order to achieve the high static low dynamic stiffness characteristic. Next the dynamic equation of the proposed system is constructed. Then, the harmonic balance method (HB) is employed to evaluate the characteristic of the motion transmissibility of the proposed system at the steady state for each of the excitation frequency. From this characteristic, the curves of the displacement transmissibility are verified based on the configurative parameters of the system.

Then, a sliding mode control (SMC) are designed for the ASVIS. The control strategy is to employ an approximate technique to express one of unknown functions to estimate the equivalent control effort. The stability of the controller is also evaluated in terms of Lyapunov theory.

Finally, numerical simulations are performed to evaluate the effectiveness of vibration isolation of the ASVIS. The results obtained in this paper show that the values of the seat displacement of the ASVIS with NSS are reduced to 77.16% in comparison with the traditional air-spring isolator without NSS, which indicates that the design of the ASVIS isolator with NSS can effectively isolate vibrations in the low-frequency region.

Chapter 1

INTRODUCTION

1.1 Background

Normally, whole-body vibration is associated with vehicle movement, which can affect the comfort, performance, and health of the vehicle driver [1, 2]. Vibrations can be transmitted to the driver from a variety of directions, as indicated in Figure 1.1, including the three longitudinal axes of x , y , and z , as well as the three rotational axes of roll, pitch, and yaw. The most severe vibration that impacts driver comfort when driving the vehicle is vibration in the low-frequency region of 1 to 20 Hz. The human body responds strongly to vertical whole-body vibration at frequencies ranging from 0.5 to 5 Hz, which are below 2 Hz in horizontal axes [3, 4]. In order to increase the comfort, safety, and health of the driver, also reduce weariness caused by extended hours of driving or exposure to adverse road conditions, a traditional vibration isolator is developed by combining a mechanical spring element in parallel to a damping element.

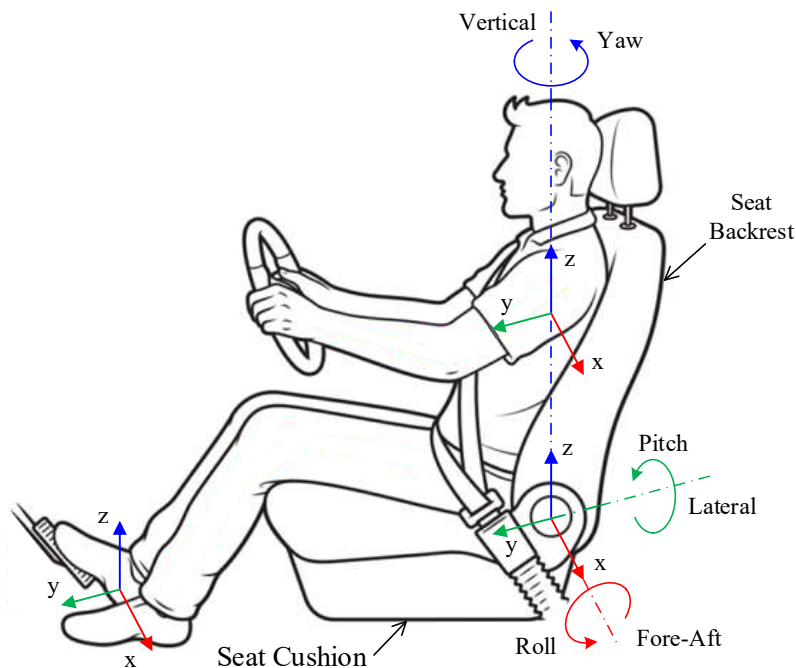


Figure 1.1. Whole body vibration of the driver

The traditional linear isolator model (Figure 1.2), which is frequently used to demonstrate vibration isolation, consists of a linear stiffness spring combined with a damper [5-7]. Only

when the excitation frequency exceeds $\sqrt{2}$ times the natural frequency of the system can these structures achieve efficient vibration isolation. On the other hand, when the excitation frequency is less than $\sqrt{2}$ times the natural frequency, the vibration of the driver's seat is increased in comparison with that of the base excitation [8]. This proves that the traditional vibration isolation systems can have a satisfying performance only at high-frequency excitation but not at low-frequency excitation.

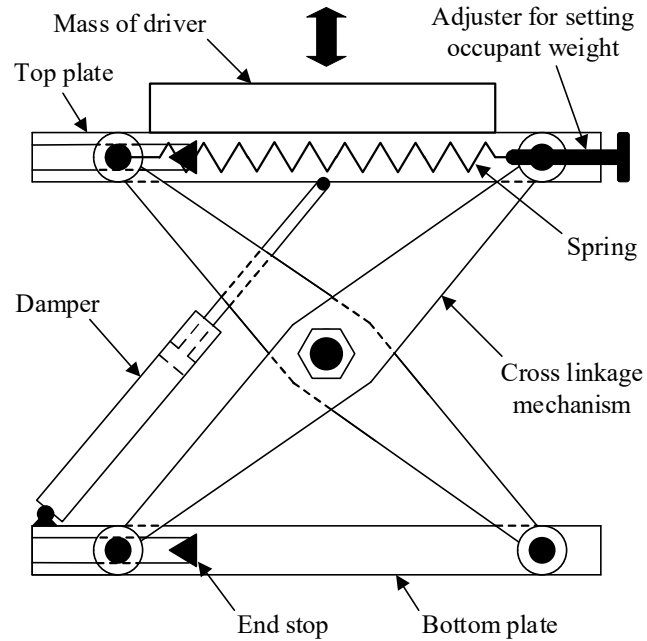


Figure 1.2. A traditional linear isolator and its component parts.

To solve this problem, vibration isolation systems with NSS have been recommended to overcome the disadvantages of classical linear isolation, which can effectively isolate vibrations in the low-frequency region while maintaining load capacity and low dynamic stiffness (Figure 1.3). In an early study by Alabuzhev et al. [9], the NSS vibration isolator comprised two horizontal springs connected to the load via an actuator joint to produce negative stiffness. Platus et al. [10] suggested a negative stiffness mechanism based on two rigid bars hinged in the middle, supported on pivots at their outer ends and loaded in compression by opposing forces. Danh et al. [11] continued to study this mechanism and developed a vibration isolator with NSS that employed two horizontal springs connected to the load via sliders and inclined links. The mechanical characteristics and experimental prototype of the proposed system were also analyzed. Later, these researchers applied an adaptive backstepping controller to enhance the isolation effectiveness of the vibration isolator system with NSS [12]. A nonlinear vibration isolation system with an NSS was investigated in terms of dynamics and

power flow by J. Yang et al. [13]. Shi et al. [14] suggested to use a novel spring bar mechanism to improve the vibration isolation performance of the NSS. Moreover, other researchers designed vibration isolation systems (Figure 1.4) that used a cam–roller mechanism combined with negative-stiffness elements [15]. Yao et al. [16] proposed a negative stiffness vibration isolator based on a cam–roller–spring mechanism with a custom-designed cam profile. Other designs that produced negative stiffness characteristics include a magnet spring structure by Zheng et al. [17] and a pneumatic negative-stiffness mechanism introduced by Palomares et al. [18]. Since the negative stiffness mechanism has very little load capacity, it can only operate well when connected in parallel with a positive-stiffness element.

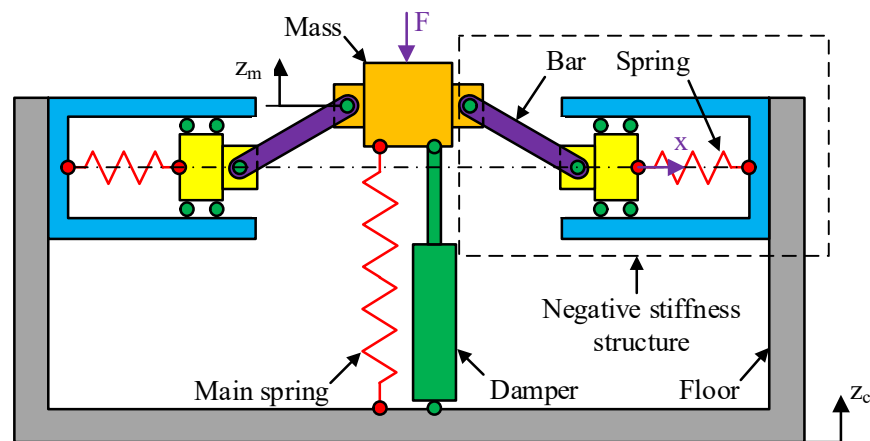


Figure 1.3. Negative stiffness structure of vehicle seat

By combining a negative-stiffness element with a positive-stiffness element in parallel, a quasi-zero-stiffness (QZS) vibration isolation system achieved both high static stiffness and low dynamic stiffness around the equilibrium position. Carrella et al. [19] proposed a QZS vibration isolator comprising a vertical spring operating in parallel with two oblique springs. Lan et al. [20] presented the nonlinear-stiffness theoretical analysis of a QZS system with damping at the dynamic equilibrium position. The results of numerical simulations of differential equations for the QZS vibration isolator under different excitations, such as harmonic excitation, random excitation, and impulse excitation, were presented by Chang et al. [21]. The vibration isolation efficiency of the QZS system was confirmed in [22], which indicated that the response of the QZS system under harmonic force was nearly almost two times lower than that of the classical linear vibration isolator. A nonlinear inertia mechanism [23] was designed by using a pair of oblique inertia with one common hinged terminal and the other terminal fixed. In addition, Zhou et al. [24] recommended a new design of the QZS

system that used a cam–roller–spring mechanism. Based on this mechanism, Ye et al. [25] further developed a QZS system with multiple frequency regions that could respond to a variety of isolated masses or applied forces. In addition, QZS vibration isolators based on linear magnetic springs [26] also attracted an attention. However, one disadvantage of the QZS vibration isolator is its limited displacement range when the stiffness is reduced to zero.

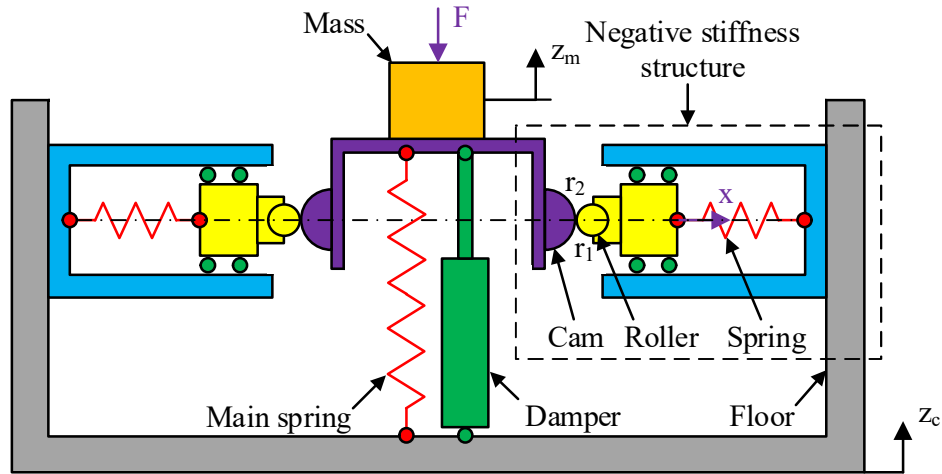


Figure 1.4. NSS with cam-roller-spring

In other studies, some researchers introduced a nonlinear vibration isolator that used a scissor-like structure (SLS) to enhance the vibration isolation effectiveness. The SLS vibration isolator described by X. Sun et al. was composed of connecting horizontal springs, rods of the same length, and joints [27]. The results demonstrated that vibration isolators with an SLS can achieve good nonlinear vibration isolation performance while simultaneously overcoming the disadvantages of an existing QZS system. Inspired by the SLS presented in [27], an innovative QZS vibration isolator was constructed, adopting a single-layer SLS and parabolic cam–roller structures [28]. The proposed vibration system showed a small improvement in offset when compared to the system with only an SLS, but significantly reduced the magnitude of the vibration. In addition, a vibration isolator with SLS was developed by Wei et al. by combining an n-layer scissor-like mechanism with electromagnetic generators [29]. The results showed that the structural parameters of the suggested system may be adjusted to obtain better energy-harvesting effectiveness. According to the above-mentioned research, the SLS can provide nonlinear stiffness, which is also effective for isolating low-frequency vibration.

On the other hand, air springs are well known for their ability to easily provide variable force and load capacities by simply adjusting the gas pressure within the springs [30]. To further enhance the isolation performance of the vehicle seat, an air spring with negative

stiffness was adopted as a vibration isolator of the driver's seat by Lee et al. [31]. Danh et al. [12] constructed a pneumatic vibration isolator employing an NSS to increase the isolation performance in low-excitation frequency ranges. Moreover, Palomares et al. [18] presented an NSS vibration isolator based on a set of two pneumatic actuators originally in a horizontal position and perpendicular to a reversible sleeve air spring. According to the analytical and experimental results, the resonance frequency of this structure was reduced by up to 58%, and the transmissibility modulus was increased by up to 78%. Furthermore, when this structure was used as a vibration isolator in vehicle seats, comfort improvements ranging from 10% to 35% were observed [32]. Hence, the pneumatic vibration isolation system based on NSS can significantly isolate the vibration at a low frequency with a different mass of the vehicle drivers.

1.2 Research objectives

The important contribution of the present paper is the replacement of the traditional vibration isolator in a vehicle seat with a new vibration isolator with NSS, which consists of two double convoluted air spring combined with a crisscross mechanism to overcome the disadvantages of the classical isolator. Furthermore, a sleeve air spring was adopted to replace a positive-stiffness spring, which provided a stable support force when the load changed. Next, a mathematical model and the relationship between the nonlinear stiffness and the displacement of the ASVIS were derived. In addition, the displacement responses with respect to the time of the ASVIS were obtained by numerical simulation to evaluate the vibration isolation performance. Then, the results were compared with those of the classical air spring isolator without NSS to show the advantages of the ASVIS with NSS. Finally, a sliding mode control will be applied to evaluate the isolation performance of the proposed system.

1.3 Contents of research

Accordingly, the developed mechanical model of the ASVIS isolator and the analysis characteristics of the air springs are presented in Section 2. The mathematical model and the stability analysis of the ASVIS are investigated in Section 3. The numerical simulation results are verified and compared with those of the classical vibration isolator without NSS in Section 4. The control method will be applied to the proposed system to the isolation performance in Section 5. Finally, Section 6 presents the conclusions and future work.

Chapter 2

DESIGN MODEL

2.1 Advantage of the air spring

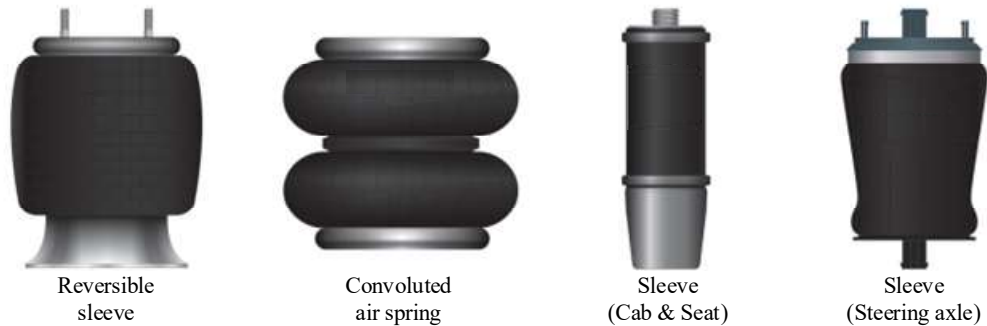


Figure 2.1 Types of air springs [33].

An air spring (or air bag) is basically a column of air confined within a rubber and fabric container. Air springs are designed and manufactured in various shapes and sizes to meet a wide variety of applications as shown in Figure 2.1. Two common types are the reversible sleeve (rolling lobe) and the convoluted (bellows) as shown in Figure 2.2. A reversible sleeve type air spring contains a piston over which the elastomeric material moves as the height of the air spring changes in relation to load variations. Thus, the piston plunges in and out of the air cavity. The convoluted air spring contains one or more bellows. There is no piston associated with this type of air spring. In general, the reversible sleeve air spring has an advantage over the convoluted by the fact that the piston can be shaped to fine tune the spring rate. In addition, it is possible with the reversible sleeve design to maintain a constant load for a given internal pressure over a range of heights [33].

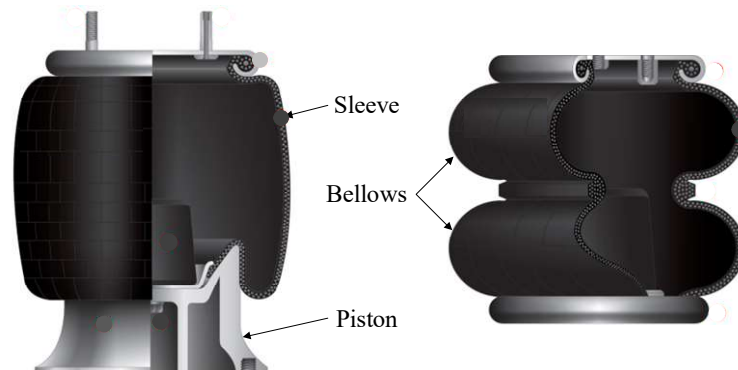


Figure 2.2. Reversible sleeve and convoluted air spring [33].

As the name implies, an air spring is typically a replacement for the traditional steel spring in a vibration isolator system. Some of the advantages enumerated in are as follows:

- + An air spring has variable load-carrying capability. If a higher load needs to be accommodated, air can be added to the spring (automatically or manually) to increase the pressure and at the same time maintain the required height of the system.
- + The spring rate of an air spring can be adjusted. When an additional load is applied, and air is added to the spring to maintain a specified height. The internal pressure increases to accommodate the load, but without a significant shift in the system natural frequency.
- + The height of the load can be adjusted when necessary by increasing or decreasing the amount of air in the air spring.
- + An air spring has low friction dynamics. Since there is a flexible elastomeric member separating the rigid attachment points of the suspension, the air spring can move in six degrees of freedom without the resistance and squeaks.

2.2 The characteristics of the air spring

2.2.1 Sleeve air spring

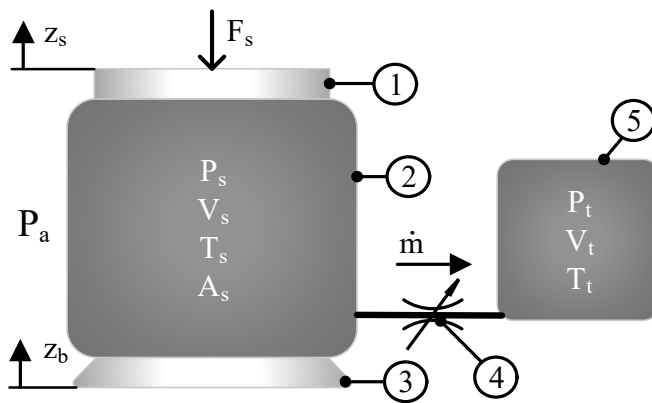


Figure 2.3. The analytical model of sleeve air spring.

Figure 2.3 illustrates the analytical model of a sleeve-type air spring, which includes bead plate (1), bellows (2), and piston (3) connected to an auxiliary tank (5) via a restrictor valve (4). When the air spring is affected by the force F_s , the gas inside the air spring is delivered from the air spring into the auxiliary tank. As a result, differential pressure is generated at both ends of the restrictor valve, causing air to flow through the restrictor valve and create damping and dissipating vibration energy. Hence, gas states in the sleeve air spring and auxiliary tank are altered, including internal air mass (kg), volume (m^3), pressure (Pa), temperature (K).

The compressed air in the bellows provides the axial sleeve air spring elastic force, which is represented by

$$F_s = (P_s - P_a) A_s \quad (2.1)$$

where P_s , P_a , and A_s are the absolute pressure of the gas in the sleeve air spring, the atmospheric pressure, and the effective area of the sleeve air spring (which is a non-linear function of the spring height), respectively.

By using the ideal gas laws, the mass flow rate of air into the sleeve air spring is expressed as follows [34]:

$$\dot{m} = \frac{d}{dt}(\rho_s V_s) = \dot{\rho}_s V_s + \rho_s \dot{V}_s \quad (2.2)$$

where the variables ρ_s and V_s are the air density and the volume of the sleeve air spring, respectively.

The mass flow rate is positive for the air inflow to the sleeve air spring and negative while exhausting the air from the sleeve air spring. Assuming that the process of air variation in the two volumes follows a polytropic process, then the relationship between air density and internal pressure is described as follows:

$$\frac{P_s}{\rho_s^n} = \frac{P_{se}}{\rho_{se}^n} \quad (2.3)$$

where the variables ρ_{se} and P_{se} represent the air density and the absolute pressure in the sleeve air spring at the equilibrium position, respectively.

The constant $n = C_p / C_v$ is the polytropic exponent, which is defined as the ratio of the specific heats of a gas. C_p and C_v are the specific heat of the gas at constant pressure and constant volume, respectively.

From the ideal gas law, the absolute pressure at equilibrium can be expressed as

$$P_{se} = \rho_{se} R T_{se} \quad (2.4)$$

where R and T_{se} are the specific gas constant and the absolute temperature at the equilibrium position, respectively.

By substituting Equation (2.4) into Equation (2.3) and differentiating with respect to time, the density of the air inside the sleeve air spring changes according to

$$\dot{\rho}_s = \frac{1}{n R T_{se}} \left(\frac{P_s}{P_{se}} \right)^{\frac{1-n}{n}} \dot{P}_s \quad (2.5)$$

By combining Equations (2.2) and (2.5), the mass flow rate is expressed as

$$\dot{m} = \frac{1}{nRT_{se}} \left(\frac{P_s}{P_{se}} \right)^{\frac{1-n}{n}} V_s \dot{P}_s + \frac{P_{se}}{RT_{se}} \left(\frac{P_s}{P_{se}} \right)^{\frac{1}{n}} \dot{V}_s \quad (2.6)$$

Then, the first-order differential equation for the pressure of the air in the sleeve air spring can be derived

$$\dot{P}_s = \frac{nRT_{se}}{V_s} \left(\frac{P_s}{P_{se}} \right)^{\frac{n-1}{n}} \dot{m} - \frac{nP_s}{V_s} \dot{V}_s \quad (2.7)$$

Expanding Equation (2.7) with Taylor's series, the change in air pressure within the sleeve air spring is described by

$$\dot{P}_s = \frac{nRT_{se}}{V_{se}} \dot{m} - \frac{nP_{se}}{V_{se}} \dot{V}_s \quad (2.8)$$

- **Auxiliary Tank**

Since the gas process in the auxiliary tank is identical to the gas process in the sleeve air spring, the differential equation for the pressure (P_t) in the auxiliary tank is derived similarly. Assume that the volume of the auxiliary tank is not changed during the operation. Based on Equation (2.2), the mass flow rate into the tank is obtained as

$$\dot{m} = -\dot{\rho}_t V_t \quad (2.9)$$

Hence, the differential equation for pressure in the auxiliary tank is written as

$$\dot{P}_t = -\frac{nRT_{te}}{V_t} \left(\frac{P_t}{P_{te}} \right)^{\frac{1-n}{n}} \dot{m} \quad (2.10)$$

where P_t and V_t are the pressure and the volume in the auxiliary tank, respectively. P_{te} and T_{te} is the pressure and temperatures in the tank at the equilibrium position, respectively.

Note that at the equilibrium position, the mass flow rate is zero ($\dot{m} = 0$), the pressures in the sleeve air spring and the auxiliary tank are equal ($P_{se} = P_{te}$). Also, the temperatures in the sleeve air spring and the auxiliary tank are assumed constant and equal ($T_{se} = T_{te}$).

- **Restrictor valve (Flow control valve)**

An equation representing restricted air flow was developed in terms of the measured upstream total pressure and temperature and the measured downstream pressure. If static pressure and temperature are measured instead of total pressure, the difference in result is

usually negligibly small. A formulation was developed that would account for both critical and subcritical flow. The mass flow rate is given by [35]

$$\dot{m}(p_u, p_d) = \begin{cases} \sqrt{\frac{2n}{R(n-1)}} \sqrt{\left(\frac{p_d}{p_u}\right)^{2/n} - \left(\frac{p_d}{p_u}\right)^{(n+1)/n}} \frac{C_q p_u}{\sqrt{T}}, & \text{if } \left(\frac{p_d}{p_u}\right) \geq P_{cr} \text{ (unchoked)} \\ \sqrt{\frac{n}{R} \left(\frac{2}{n+1}\right)^{(n+1)/(n-1)}} \frac{C_q p_u}{\sqrt{T}} & \text{if } \left(\frac{p_d}{p_u}\right) \leq P_{cr} \text{ (choked)} \end{cases} \quad (2.11)$$

where C_q , p_d / p_u , and P_{cr} are the flow coefficient, the flow type depends on the pressure ratio, and the critical pressure ratio, respectively.

2.2.2 Convoluted air spring

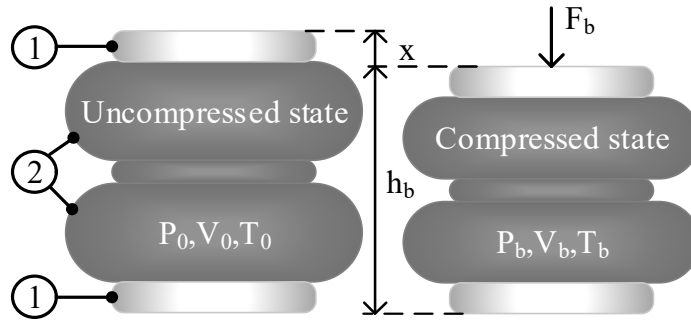


Figure 2.4. The analytical model of convoluted air spring.

Consider a convoluted air spring as displayed in Figure 2.4. It can be shown that this spring is compressed by approximately x from its uncompressed state. By applying the first law of thermodynamics, the relationship between the force F_b and the pressure on the convoluted air spring is as follows [36]

$$F_b = (P_b - P_a) \cdot A_b \quad (2.12)$$

where P_b is the absolute pressure in the convoluted air spring, and A_b is the effective area of the convoluted air spring.

The stiffness characteristic of the convoluted air spring can be defined as the derivative of this force with respect to the height x according to Equation (2.13)

$$K_b = \frac{dF_b}{dx} = (P_b - P_a) \frac{dA_b}{dx} + \frac{d(P_b - P_a)}{dx} A_b \quad (2.13)$$

If it is assumed that the change in gas conditions is a polytropic process, the thermodynamic state of air in the bellows is described by

$$P_b V_b^n = \text{constant} \quad (2.14)$$

Given the initial absolute pressure P_0 and volume V_0 , the volume of the convoluted air spring V_b at an absolute pressure P_b is defined by Equation (2.15)

$$V_b = V_0 \left(\frac{P_0}{P_b} \right)^{\frac{1}{n}} \quad (2.15)$$

The derivative of the absolute pressure P_b with respect to the height h can be derived from Equation (2.14)

$$\frac{dP_b}{dx} = - \frac{n \cdot P_b \cdot V_b^{n-1}}{V_b^n} \frac{dV_b}{dx} \quad (2.16)$$

Combining Equation (2.16) with Equation (2.13), we can obtain the stiffness of the convoluted air spring as

$$K_b = (P_b - P_a) \frac{dA_b}{dx} - \frac{n P_b A_b}{V_b} \frac{dV_b}{dx} \quad (2.17)$$

2.3 Model description

The ASVIS with NSS was improved with respect to the traditional vibration isolator by employing a sleeve air spring to replace the damper and the mechanical linear spring. The general structure of the ASVIS is displayed in Figure 2.5. It consists of three individual structures, namely, a convoluted air spring with NSS (1), a crisscross mechanism (2), and a sleeve-type air spring (3). When the isolated object (4) moves vertically, the air bellows mechanism (1) combines with the crisscross mechanism (2) to provide negative stiffness along the vertical axis, while a sleeve air spring (3) provides positive stiffness.

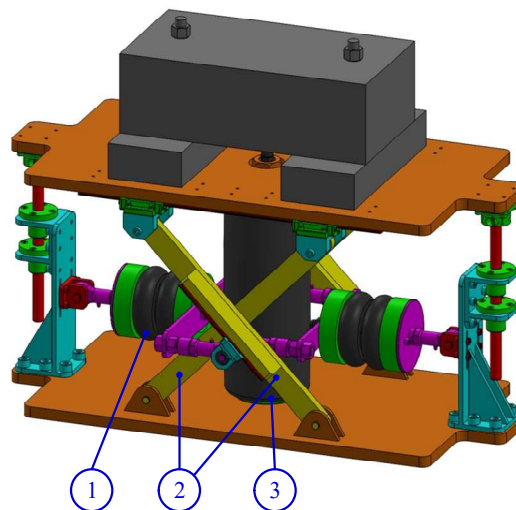


Figure 2.5. The general structure of the ASVIS model

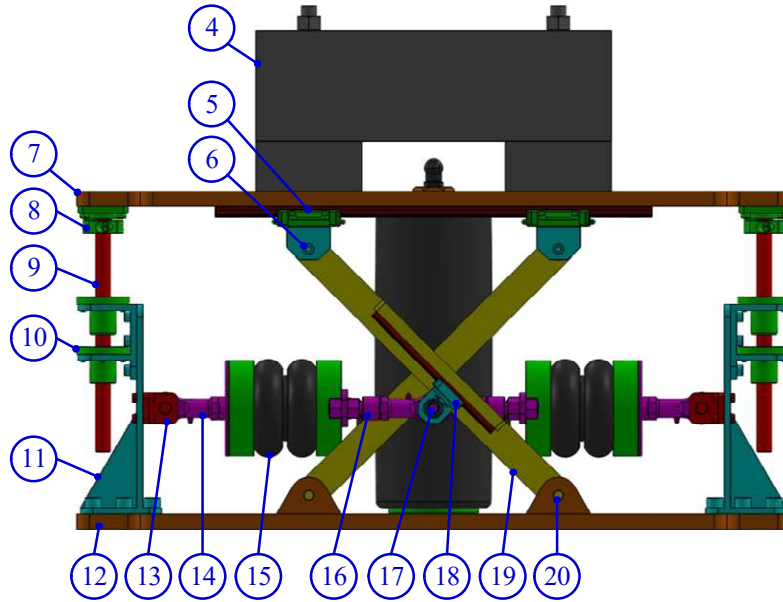


Figure 2.6. Schematic diagram of ASVIS at the static equilibration position

1. Negative stiffness structure; 2. crisscross structure; 3. sleeve air spring; 4. isolated object; 5. upper linear guide; 6. linear support; 7. upper plate; 8. bracket; 9. linear shaft; 10. linear bushings; 11. base support; 12. base; 13. bellows fork; 14. left link; 15. air bellows; 16. right link; 17. rotating joint; 18. bellows linear guide; 19. straight bar; 20. pin.

The schematic diagram of the ASVIS in the static equilibration position is described in Figure 2.6. Firstly, the isolated object (4) was fixed to the upper plate and kept stationary. Two linear shafts (9) were assembled perpendicularly to the upper plate (7) by a bracket (8), which could slip on the two linear bushings (10). The two linear bushings (10) were fitted on the base support (11) to make the upper plate (7) move only along the vertical direction. Moreover, a crisscross structure (2) comprised two straight bars (19) and loading support in a crisscross ‘X’ pattern. The upper ends of the straight bar (19) were connected with the upper linear guide (5) via a linear support (6), while the lower ends of the straight bar (19) were connected in the same manner to the base (12). Hence, the lower ends of the straight bar (19) could rotate circularly by means of a pin (20), while the upper ends could freely slide along the surface of the upper plate (7). Furthermore, two air bellows (15) were installed between the left link (14) and the right link (16). One side of the air bellows (15) was connected with a bellows fork (13), and the other side was connected with the crisscross mechanism by using a rotating joint (17). This joint could move up and down while slipping on the bellows linear guide (18). Finally, the NSS consisted of the air bellows (15), the bellows fork (13), the left link (14), and the right link (15), which produced a negative stiffness in the vertical direction.

The two convoluted air springs provide the negative stiffness necessary to counteract the positive stiffness of the vertical spring and achieve the desired negative stiffness characteristic. In addition, a sleeve air spring was also added since it could provide sufficient rigidity in static conditions and be adapted to any weight changes. As a result, the dynamic stiffness in the vertical axis of the ASVIS system was equal to the total of the dynamic stiffness of the sleeve-type air spring and the negative-stiffness structure.

Moreover, the air-bellows springs are symmetrically designed so that they remain horizontal when the isolated object is static. The sleeve-type air spring is also included as it provides adequate rigidity in static conditions and may also be adapted to any weight changes. When the isolated object is moving up and down, the air bellows spring provides negative stiffness along the vertical direction, while the sleeve air spring offers positive stiffness. Hence, the total dynamic stiffness of the vibration isolator is determined by the sum of the dynamic stiffness of the air-bellows spring and the sleeve air spring.

2.4 Conclusions

In this chapter, it has been shown that by connecting pneumatic springs with positive and negative stiffness in parallel it is possible to design a vibration isolation system that has high static stiffness, small static deflection, and a low natural frequency, a wider isolation region. Systems with these properties have been termed ASVIS mechanisms and offer potential improvements in the isolation performance of vehicle seats. In addition, the advantages of the proposed system over the system based on conventional mechanical springs include:

- + Adjustable carrying capacity
- + Reduced weight
- + Variable spring rate with constant “tuned” frequency
- + Reduced structurally transmitted noise
- + Variability of ride heights.

In the remaining chapters, both nonlinear and linear behavior will be further analyzed: in Chapter 3, a nonlinear analysis will be carried out in order to predict the system dynamics when the linear approximation is no longer applicable, whereas in chapter 4 the performance of the proposed system will be validated via simulating. In chapter 5, the control method and results will be presented.

Chapter 3

Analysis of ASVIS

3.1 Static analysis

In this chapter, the concept of negative stiffness is illustrated and two structures of the ASVIS are introduced and discussed. The first system comprises two straight bars operating in parallel with two convoluted air springs. The two convoluted air springs provide the negative stiffness necessary to counteract the mass of the isolation object and achieve the desired negative stiffness characteristic. In the second mechanism, the positive stiffness is provided by a set of a sleeve air-spring. The analysis carried out in this chapter aims to define the expressions for the force and stiffness as functions of the displacement and to describe the parameters that influence the systems' ASVIS property. Finally, the motion equation of the proposed system is presented.

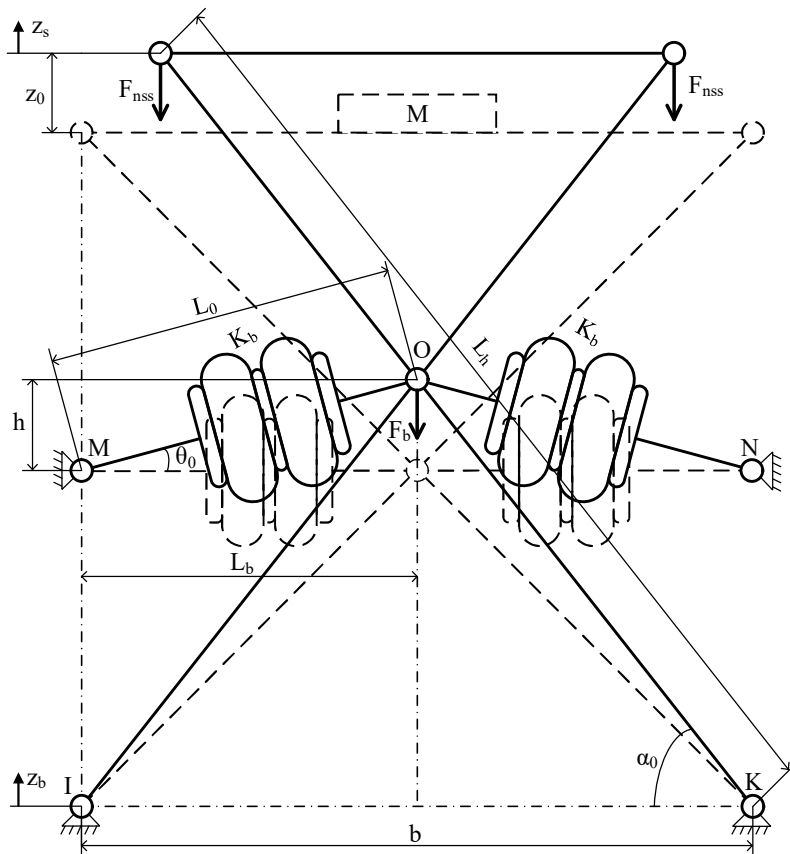


Figure 3.1. Schematic diagram of the NSS and the crisscross structure.

The schematic of the crisscross structure and negative stiffness mechanism without the sleeve air spring with stiffness K_s is displayed in Figure 3.1. The solid line indicates the initial position of the ASVIS, meaning that at this position, two bellows air springs and a sleeve air spring were uncompressed. The dashed line describes the static equilibrium position of the ASVIS when an isolated object with mass (M) is placed on the upper plate. In this diagram, z_b and z_s are the absolute displacements of the isolated object and the base excitation, respectively, and z_0 is the vertical static distance between the static equilibrium position and the highest position, which corresponds to the condition with no isolated object. Moreover, L_h is the length of the two straight bars of the crisscross mechanism, and α is the angle that each straight bar makes with the horizontal direction. The horizontal distance between two rotation joints at points I and K is denoted by the symbol b . Two convoluted air springs, which are initially located at an angle θ_0 from the horizontal direction, have a stiffness K_b at points M and N. A force F_b is exerted by the convoluted air spring on point O, which is horizontally distanced L_b from the points M and N, while initially located at a height h from these points.

Based on the geometrical relationships in the crisscross structure, the static distance z_0 caused by mass M is obtained as

$$z_0 = 2h - (b - L_h \cos \alpha) \tan \alpha \quad (3.1)$$

The increment of the length of the convoluted air spring can be written as

$$\Delta L_b = L_0 - L_b = \sqrt{h^2 + L_b^2} - L_b \quad (3.2)$$

where L_0 is the length of the convoluted air spring in an uncompressed state, and L_b is its length in the static equilibrium position.

The force provided by the convoluted air spring F_b is derived as

$$F_b = 2K_b \Delta L_b \sin \theta \quad (3.3)$$

where K_b is the stiffness of the spring, and $\sin \theta = h / \sqrt{h^2 + L_b^2}$.

We can describe (3.3) as follows

$$F_b = 2K_b h \left(1 - \frac{L_b}{\sqrt{h^2 + L_b^2}} \right) \quad (3.4)$$

In the vertical direction, the total force F_{nss} supplied by the convoluted air spring can be expressed by

$$F_{nss} = 2F_b \cos \alpha / \cos \alpha_0 \quad (3.5)$$

where $\cos \alpha_0 = b / L_h$ is the initial angle of a straight bar with the horizontal direction.

Substituting Equations (3.1) and (3.4) into Equation (3.5) the general equation for the relationship between force F_{nss} and distance z_0 in the vertical direction is as follows

$$F_{nss} = \left(\frac{2K_b \cos \alpha (z_0 + (b - L_h \cos \alpha) \tan \alpha)}{\cos \alpha_0} \right) \left(1 - \frac{L_b}{\sqrt{\left(\frac{z_0 + (b - L_h \cos \alpha) \tan \alpha}{2} \right)^2 + L_b^2}} \right) \quad (3.6)$$

The dimensionless parameters are defined as follows

$$\hat{F}_{nss} = \frac{F_{nss}}{K_b L_b}; \quad \hat{z}_0 = \frac{z_0}{L_b}; \quad \hat{L}_h = \frac{L_h}{L_b}; \quad \text{and} \quad \hat{b} = \frac{b}{L_b}$$

where \hat{F}_{nss} , \hat{z}_0 , \hat{L}_h , and \hat{b} are the non-dimensional restoring force, the non-dimensional distance of z_0 , the non-dimensional length of the straight bar L_h , and the non-dimensional distance of b , respectively.

Replacing \hat{z}_0 , \hat{L}_h , and \hat{b} into Equation (3.6), the non-dimensional restoring force of the NSS can be written as

$$\hat{F}_{nss} = \left(\frac{2 \cos \alpha (\hat{z}_0 + (\hat{b} - \hat{L}_h \cos \alpha) \tan \alpha)}{\cos \alpha_0} \right) \left(1 - \frac{1}{\sqrt{\left(\frac{\hat{z}_0 + (\hat{b} - \hat{L}_h \cos \alpha) \tan \alpha}{2} \right)^2 + 1}} \right) \quad (3.7)$$

Differentiating Equation (3.6) with respect to the distance z_0 yields the stiffness of the ASVIS as follows

$$K_{nss} = \frac{2K_b \cos \alpha}{\cos \alpha_0} \left(1 - \frac{L_b}{\sqrt{\left(\frac{z_0 + (b - L_h \cos \alpha) \tan \alpha}{2} \right)^2 + L_b^2}} + \frac{\frac{L_b}{2} (z_0 + (b - L_h \cos \alpha) \tan \alpha)^2}{\sqrt{\left(\left(\frac{z_0 + (b - L_h \cos \alpha) \tan \alpha}{2} \right)^2 + L_b^2 \right)^3}} \right) \quad (3.8)$$

The non-dimensional stiffness $\hat{K}_{nss} = K_{nss} / K_b L_b$ can be expressed as

$$\hat{K}_{nss} = \frac{2 \cos \alpha}{\cos \alpha_0} \left(1 - \frac{1}{\sqrt{\left(\frac{\hat{z}_0 + (\hat{b} - \hat{L}_h \cos \alpha) \tan \alpha}{2} \right)^2 + \hat{L}_b^2}} + \frac{\frac{1}{2} (\hat{z}_0 + (\hat{b} - \hat{L}_h \cos \alpha) \tan \alpha)^2}{\sqrt{\left(\left(\frac{\hat{z}_0 + (\hat{b} - \hat{L}_h \cos \alpha) \tan \alpha}{2} \right)^2 + \hat{L}_b^2 \right)^3}} \right) \quad (3.9)$$

For the negative stiffness structure and crisscross structure in Figure 3.1, the sleeve air spring (K_s) is in parallel with the vertical components of the convoluted air spring. The reaction force of the sleeve air spring is given by

$$F_s = K_s z_0 \quad (3.10)$$

The equivalent force of the ASVIS can be written as

$$F_{eq} = F_s + 2F_{nss} \quad (3.11)$$

The non-dimensional equivalent force of the ASVIS is obtained as

$$\hat{F}_{eq} = \hat{z}_0 + \left(\frac{2\hat{K}_{bs} \cos \alpha (\hat{z}_0 + (\hat{b} - \hat{L}_h \cos \alpha) \tan \alpha)}{\cos \alpha_0} \right) \left(1 - \frac{1}{\sqrt{\left(\frac{\hat{z}_0 + (\hat{b} - \hat{L}_h \cos \alpha) \tan \alpha}{2} \right)^2 + 1}} \right) \quad (3.12)$$

where $\hat{K}_{bs} = K_b / K_s$ is the ratio of the stiffness of the convoluted air spring to that of the sleeve air spring.

The non-dimensional stiffness of the ASVIS is determined by differentiating the equivalent force F_{eq} depending on the distance z_0 as follows

$$\hat{K}_{eq} = 1 + \frac{2\hat{K}_{bs} \cos \alpha}{\cos \alpha_0} \left(1 - \frac{1}{\sqrt{\left(\frac{\hat{z}_0 + (\hat{b} - \hat{L}_h \cos \alpha) \tan \alpha}{2} \right)^2 + 1}} + \frac{1/2 (\hat{z}_0 + (\hat{b} - \hat{L}_h \cos \alpha) \tan \alpha)^2}{\sqrt{\left(\left(\frac{\hat{z}_0 + (\hat{b} - \hat{L}_h \cos \alpha) \tan \alpha}{2} \right)^2 + 1 \right)^3}} \right) \quad (3.13)$$

At the static equilibrium position it can be positive, zero or negative depending on the values of the system's parameters α and z_0 . The combination of these two parameters that gives zero

stiffness at the equilibrium position is found by setting the stiffness to zero when $z_0 = 0$ and $\alpha = \alpha_0 = \pi/4$ as

$$\hat{K}_{eq} = 1 + 2\hat{K}_{bs} \left(1 - \frac{1}{4\sqrt{(2\hat{b} - \sqrt{2}\hat{L}_h)^2 + 16}} + \frac{(2\hat{b} - \sqrt{2}\hat{L}_h)^2}{512\sqrt{\left((2\hat{b} - \sqrt{2}\hat{L}_h)^2 + 16\right)^3}} \right) \quad (3.14)$$

3.2 Dynamic analysis

Assume the base of a proposed system undergoes harmonic motion, $z_b = Z_b \cos(\omega t)$, the displacement of the isolated object z_s from its static equilibrium position at the time t . The displacement of the isolated object relative to the vehicle frame described by

$$z = z_s - z_b \quad (3.15)$$

Considering the sleeve-type air spring as a viscous damper c with a linear spring k . The equation of motion of ASVIS system can be written in the form

$$m\ddot{z} + c\dot{z} + kz + f_{nss} = -m\ddot{z}_b \quad (3.16)$$

The restoring force of the system can be expressed as a power series of order third can be expressed as

$$f = f(z_0) + \sum_{n=1}^3 \frac{f^n(z_0)}{n!} (z - z_0)^n \quad (3.17)$$

where $f^n(z_0)$ denotes the n^{th} derivative of “ f ” evaluated at the point a .

Since the system is designed to oscillate about the static equilibrium position it is of interest to expand the force characteristic around this point. Using a Taylor series expansion in Equation (3.17), an approximate expression for the nondimensional force can be obtained as

$$\hat{f}(\hat{z}) = \delta^2 \hat{z} + \gamma z^3 \quad (3.18)$$

The motion of ASVIS system can be written as follows

$$m\ddot{z} + c\dot{z} + kz + \gamma z^3 = -m\ddot{z}_b \quad (3.19)$$

A sinusoidal exaction is considered as

$$\ddot{z}_b = \omega^2 Z_b \cos \omega t \quad (3.20)$$

where Z_b is the excitation amplitude, ω is the excitation frequency.

The non-dimensional form of the equation of motion is as follows

$$\ddot{\hat{z}} + 2\zeta\dot{\hat{z}} + \hat{z} + \alpha\hat{z}^3 = \Omega^2 \cos \Omega \tau \quad (3.21)$$

where

$$\ddot{\hat{z}} = \frac{\ddot{z}}{\omega_n^2 Z_b}; \quad \dot{\hat{z}} = \frac{\dot{z}}{\omega_0 Z_b}; \quad \hat{z} = \frac{z}{Z_b}; \quad \alpha = \frac{\gamma Z_b^2}{k}$$

$$\zeta = \frac{c}{2m\omega_n}; \quad \omega_n^2 = \frac{k}{m}; \quad \Omega = \frac{\omega}{\omega_n}; \quad \tau = \omega_n t$$

with the t denoting differentiation with respect to non-dimensional time τ .

An approximate solution to the equation of motion can be derived by applying the Harmonic Balance method in [37], which is based on the assumption that the response (in this case the relative displacement) is harmonic at the excitation frequency and can be represented as

$$\hat{z} = \hat{Z} \cos(\Omega \tau + \phi) = \hat{Z} \cos \phi \quad (3.22)$$

which implies

$$\begin{cases} \dot{\hat{z}} = -\Omega \hat{Z} \sin \phi \\ \ddot{\hat{z}} = -\Omega^2 \hat{Z} \cos \phi \end{cases} \quad (3.23)$$

where \hat{Z} and ϕ are constants to be determined. \hat{Z} and ϕ denote the amplitude and phase angle of the response, respectively. By substituting Equation (3.22) and (3.23) into Equation (3.21), we arrive at

$$-\Omega^2 \hat{Z} \cos(\Omega \tau + \phi) - 2\zeta \Omega \hat{Z} \sin(\Omega \tau + \phi) + \alpha \hat{Z}^3 \cos^3(\Omega \tau + \phi) = \Omega^2 \cos \Omega \tau \quad (3.24)$$

Using the trigonometric relations

$$\cos^3 \phi = \frac{1}{4}(3 \cos \phi + \cos 3\phi) \approx \frac{3}{4} \cos \phi \quad (3.25)$$

The harmonic motion can be rearranged as

$$\Omega^2 \cos(\Omega \tau) = \Omega^2 \cos(\phi - \phi) = \Omega^2 (\cos \phi \cos \phi + \sin \phi \sin \phi) \quad (3.26)$$

Finally, inserting Equations(3.25) and (3.26) into Equation (3.24) gives

$$-\Omega^2 \hat{Z} \cos \phi - 2\zeta \Omega \hat{Z} \sin \phi + \hat{Z} \cos \phi + \frac{3}{4} \alpha \hat{Z}^3 \cos \phi = \Omega^2 (\cos \phi \cos \phi + \sin \phi \sin \phi) \quad (3.27)$$

Equating the coefficients of similar functions yields the system of two coupled algebraic equations

$$\begin{cases} \frac{3}{4} \alpha \hat{Z}^3 + (1 - \Omega^2) \hat{Z} = \Omega^2 \cos \phi \\ -2\zeta \Omega \hat{Z} = \Omega^2 \sin \phi \end{cases} \quad (3.28)$$

By squaring and adding both Equations (3.28) which results in

$$\frac{9}{16}\alpha^2\hat{Z}^6 + \frac{3}{2}(1-\Omega^2)\alpha\hat{Z}^4 + \left((1-\Omega^2)^2 + 4\zeta^2\Omega^2\right)\hat{Z}^2 = \Omega^4 \quad (3.29)$$

Which can also be written as

$$(\hat{Z}^2 - 1)\Omega^4 + \left((4\zeta^2 - 2)\hat{Z}^2 - \frac{3\alpha}{2}\hat{Z}^4\right)\Omega^2 + \frac{9}{16}\alpha^2\hat{Z}^6 + \frac{3}{2}\alpha\hat{Z}^4 + \hat{Z}^2 = 0 \quad (3.30)$$

Solving Equation (3.30) for Ω yields

$$\left\{ \begin{array}{l} \Omega_1 = \sqrt{\frac{\sqrt{3\alpha\hat{Z}^4 + 4\hat{Z}^2(1-2\zeta^2)} - \hat{Z}\sqrt{(3\alpha\hat{Z}^2 + 4)^2 - 64\hat{Z}^2\zeta^2(1-\zeta^2)} - 48\alpha\zeta^2\hat{Z}^4}{4(\hat{Z}^2 - 1)}} \\ \Omega_2 = \sqrt{\frac{\sqrt{3\alpha\hat{Z}^4 + 4\hat{Z}^2(1-2\zeta^2)} + \hat{Z}\sqrt{(3\alpha\hat{Z}^2 + 4)^2 - 64\hat{Z}^2\zeta^2(1-\zeta^2)} - 48\alpha\zeta^2\hat{Z}^4}{4(\hat{Z}^2 - 1)}} \end{array} \right. \quad (3.31)$$

If the radicand of the nested square root is negative then Ω_1 and Ω_2 become complex. Thus, for Ω_1 and Ω_2 to be positive, the following condition has to hold

$$(3\alpha\hat{Z}^2 + 4)^2 - 64\hat{Z}^2\zeta^2(1-\zeta^2) - 48\alpha\zeta^2\hat{Z}^4 > 0 \quad (3.32)$$

In order to extract simple expressions, we assume that the damping is small ($\zeta^2 \ll 1$). Equation (3.32) can be solved for the response amplitude to give four values of \hat{Z} . Hence, the only real positive value is

$$\hat{Z} < \hat{Z}_{\max} \quad (3.33)$$

where

$$\hat{Z}_{\max} = 2\sqrt{\frac{8\zeta^2\left(1 - \sqrt{1 + \frac{3\alpha}{4}}\right) - 3\alpha}{3\alpha(3\alpha - 16\zeta^2)}} \quad (3.34)$$

which can be further simplified if it imposed that α is 'small', in which case Equation (3.34) becomes

$$\hat{Z}_{\max} \approx \frac{2}{\sqrt{16\zeta^2 - 3\alpha}} \quad (3.35)$$

The principal parameter for the inspection of the isolation properties of the vibration isolator is the absolute transmissibility which is defined as the ratio between the displacement of the object and that of the base,

$$|T_m| = \frac{|z_s|}{|z_b|} \quad (3.36)$$

where the subscript m is used to indicate that this is the absolute motion transmissibility.

This is related to the relative transmissibility as follows

$$|T_m| = \frac{|z_s - z_b + z_b|}{Z} = \frac{|z + z_b|}{Z} \quad (3.37)$$

The vectors z and z_b rotate at the same angular speed but with a phase lag ϕ . When divided by Z their modulus become \hat{Z} and 1, respectively. Hence, the absolute motion transmissibility is the sum of two vectors with magnitude \hat{Z} and 1 at an angle ϕ . The modulus of the resulting vector is

$$|T_m| = \sqrt{1 + 2\hat{Z} \cos \phi + \hat{Z}^2} \quad (3.38)$$

where $\cos \phi$ is determined directly from the application of the HB method and is given by

$$\cos \phi = \frac{(1 - \Omega^2 + 3/4\alpha Z^2)Z}{\Omega^2} \quad (3.39)$$

Substituting Equation (3.39) into Equation (3.38) the absolute transmissibility is thus given by

$$|T_m| = \sqrt{1 + \hat{Z}^2 + \frac{2\hat{Z}^2}{\Omega^2} \left(1 - \Omega^2 + \frac{3}{4}\alpha \hat{Z}^2\right)} \quad (3.40)$$

where Ω is a function of \hat{Z} according to Equation (3.31). From Equation (3.40) it can be seen that the absolute transmissibility reaches its maximum when $\hat{Z} = \hat{Z}_{\max}$. Hence

$$|T_m|_{\max} = \sqrt{1 + \hat{Z}_{\max}^2 + \frac{2\hat{Z}_{\max}^2}{\Omega^2} \left(1 - \Omega^2 + \frac{3}{4}\alpha \hat{Z}_{\max}^2\right)} \quad (3.41)$$

Having assumed that $\zeta^2 \ll 1$ the approximate expression for the peak absolute transmissibility is found to be

$$|T_m|_{\max} \approx \sqrt{1 + \frac{4}{16\zeta^2 - 3\alpha}} \quad (3.42)$$

3.3 Conclusions

In this chapter, static response at the equilibration position of the proposed system have been established. In addition, the functions that describe the force and stiffness relationship with respect to displacement have been expressed with the symmetric polynomial. In particular, the parameters that influence the system's dynamic stiffness property has been evaluated. Furthermore, the dynamic response and absolute transmissibility of the ASVIS with negative stiffness to a harmonic excitation of the base have been investigated.

From this analysis, the relationship between the nonlinear stiffness and configurative parameters of the system is derived. It reveals that the nonlinear stiffness curve is a convex or concave parabola depending on the selection of the configurative parameters. In order to guarantee the load-bearing capacity, the nonlinear stiffness curve must be concave.

Chapter 4

SIMULATIONS RESULTS

4.1 Numerical simulation

The non-dimensional restoring force curves and the non-dimensional restoring stiffness curves are depicted in Figure 4.1 based on Equations (3.7) and (3.9) to demonstrate the effects of the angle α on the proposed system's parameters. Figure 4.1(a) shows the simulation results of \hat{F}_{nss} and \hat{z} for different values of α . Although it is demonstrated that changing the angle α causes the stiffness curves to shift horizontally, their shape is not changed. In Figure 4.1(b), the stiffness of the NSS in the small displacement range increases with the increase in displacement.

As a result, the non-dimensional reaction forces generated by NSS are equal to zero and change direction nearby the equilibrium position. In addition, the negative stiffness of the system is symmetrical and reaches the minimum at this position. Furthermore, as the displacement value \hat{z} moves away from the equilibrium position, both the force and the stiffness increase. Hence, the zero stiffness can be achieved at the equilibrium position while the angle α is chosen appropriately.

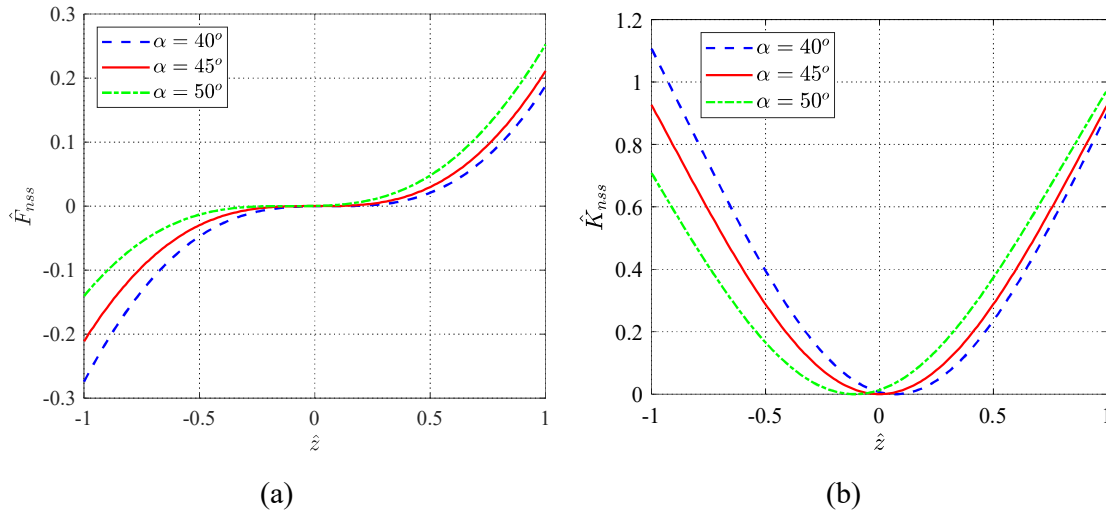


Figure 4.1. Non-dimensional force and non-dimensional stiffness of the NSS with $\hat{L}_h = \sqrt{2}$ and $\hat{b} = 1$. (a) Non-dimensional force; (b) Non-dimensional stiffness.

From the non-dimensional stiffness curves for the different \hat{L}_h and \hat{b} in Figure 4.2, we discovered that the NSS was realized under various stiffness characteristics. As the value \hat{L}_h and the displacement response \hat{b} changed, the non-dimensional restoring stiffness moved around the static equilibrium position. Thus, if the values of \hat{L}_h and \hat{b} are chosen correctly, they can provide negative stiffness over the entire displacement range.

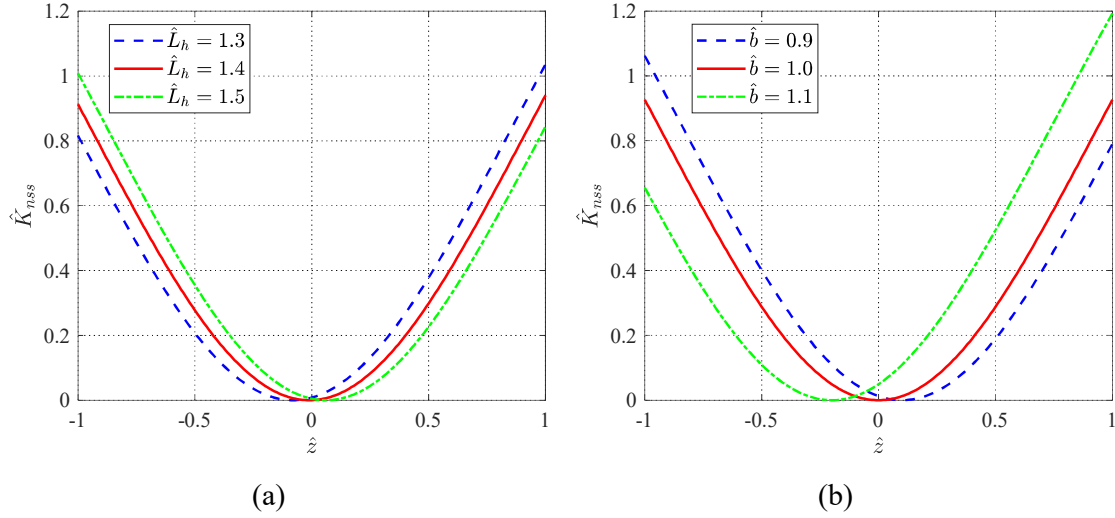


Figure 4.2. Non-dimensional stiffness of the NSS for different \hat{L}_h and \hat{b} with $\alpha = 45^\circ$.
 (a) Non-dimensional stiffness for different \hat{L}_h ; (b) non-dimensional stiffness for different \hat{b} .

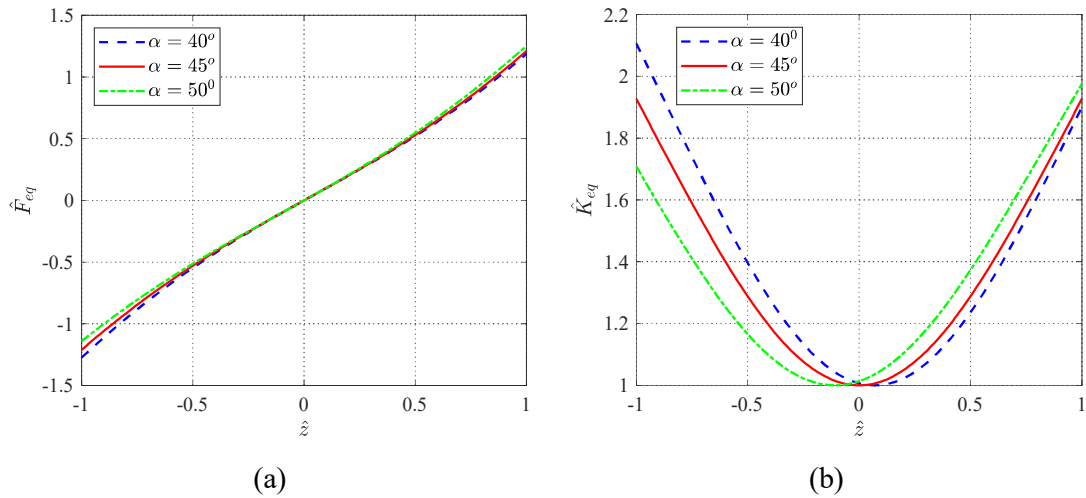


Figure 4.3. Non-dimensional force and non-dimensional stiffness of the ASVIS with NSS.
 (a) Non-dimensional force; (b) non-dimensional stiffness.

We obtained the non-dimensional restoring forces and the non-dimensional restoring stiffness of the ASVIS with NSS, as shown in Figure 4.3, with dimensionless parameters such

as $K_{bs} = 1$, $\hat{b} = 1$, and $\hat{L}_h = 2$. Figure 4.3 presents the non-dimensional restoring forces of the proposed isolator when the angle α changed. As can be seen from Figure 4.3, the minimum stiffness of the proposed system was equal to zero at the equilibrium position for $\alpha = 45^\circ$. Moreover, the non-dimensional stiffness increased when enhancing the deviation from the equilibrium position. Hence, the dynamic stiffness of the isolator always increased, except at one position where it was zero. This means we should reasonably choose a value α to provide high isolation efficiency in the actual conditions.

Moreover, the dimensionless nonlinear stiffness \hat{K}_{eq} is a minimum value at the static equilibrium position. As the stiffness \hat{K}_{eq} is increased, the fundamental frequency is also increased. This leads to a low-frequency bandwidth of isolation. When \hat{K}_{eq} is equal to one, the fundamental frequency of the proposed system is nearly equal to the natural frequency of the system without NSS.

4.2 Responses and isolation performance

4.2.1 Simulation setup

In order to confirm the vibration isolation ability of the proposed isolator, we compared it with the classical vibration isolator without NSS. Based on Newton's second law, the motion equation of the ASVIS with NSS

$$m\ddot{z} = -mg + F_s + 2F_{nss} \quad (4.1)$$

where F_{nss} and F_s are the response forces of the negative-stiffness structure in Equation (3.6) and of the sleeve-type air spring in Equation (3.10), respectively.

The operating height of the sleeve-type air spring is considered based on their relative displacement and height at the equilibrium position as follows

$$L_h = L_{se} + (z_s - z_b) \quad (4.2)$$

Similarly, the activity height of the double-convoluted bellows is given as

$$h_b = h_{be} + \Delta L_b \quad (4.3)$$

where L_{he} and h_{be} are the height of the sleeve-type air spring and the convoluted air spring at the equilibrium position, respectively.

The effective area and volume of the sleeve-type air-spring are described by a quadratic polynomial as follows [38]:

$$\begin{aligned}
A_s(L_h) &= -5.9027L_h^3 + 3.4464L_h^2 - 0.6498L_h + 0.0445 \\
V_s(L_h) &= -0.0041L_h^2 + 0.007L_h - 0.000213
\end{aligned}
\tag{4.4}$$

Similarly, the effective area and volume of the convoluted air spring were obtained according to

$$\begin{aligned}
A_b(h_b) &= -5.3157h_b^3 + 1.714h_b^2 - 0.2254h_b + 0.024 \\
V_b(h_b) &= -0.018h_b^2 + 0.0168h_b - 0.000357
\end{aligned}
\tag{4.5}$$

The air springs used in the ASVIS with NSS were a reversible sleeve model of the Firestone [Appendix I] and a double-bellows actuator of Festo [Appendix II]. The data simulation for both types of the air springs in this thesis is presented in Table 4.1, while effective area and volume graphs are shown in Figures 4.4-4.7.

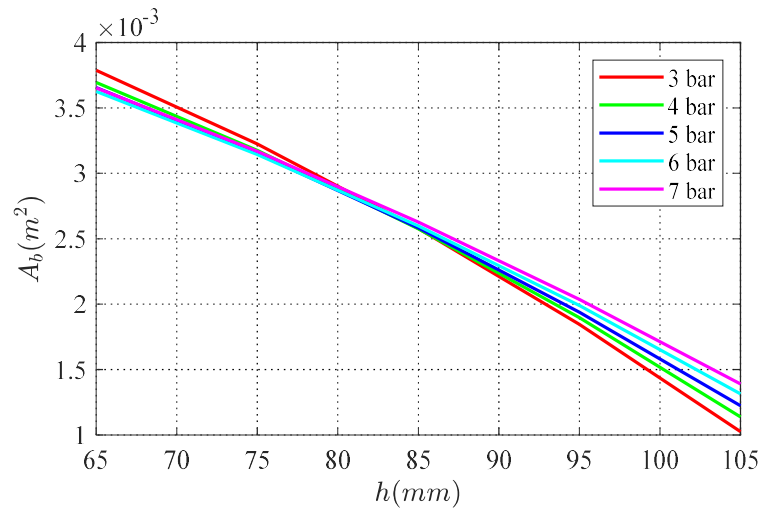


Figure 4.4. The effective area of the double-convoluted bellows.

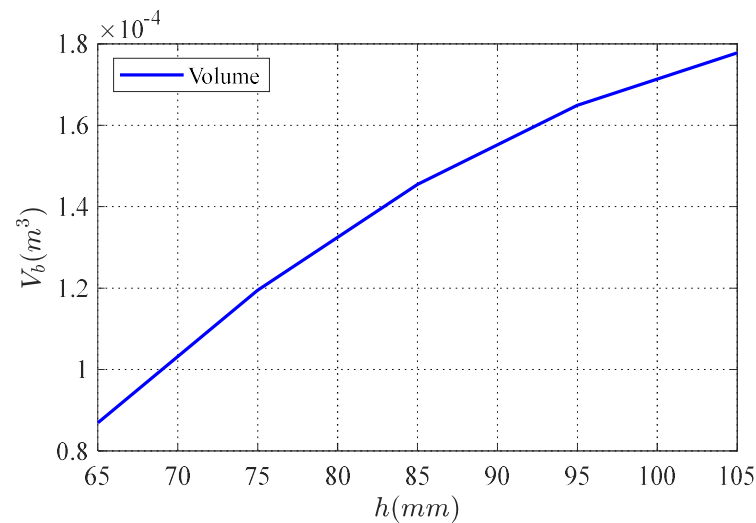


Figure 4.5. The volume of the double-convoluted bellows at the pressure 7 bar.

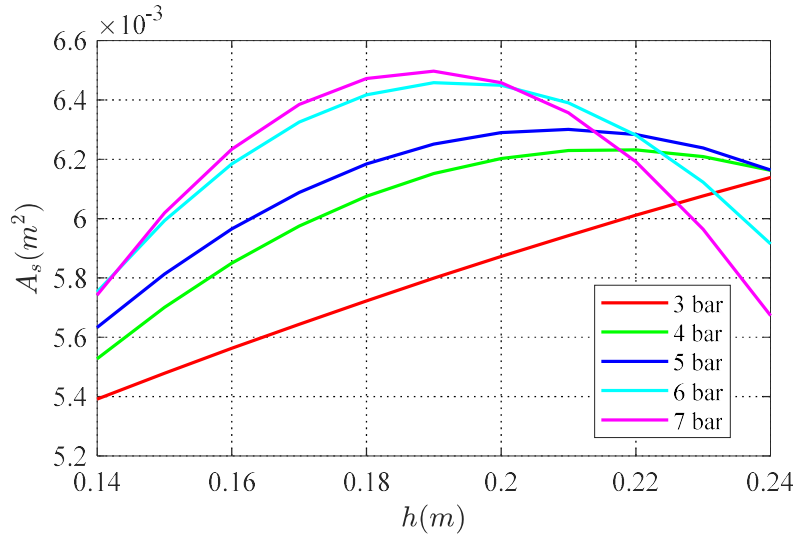


Figure 4.6. The effective area of the sleeve air spring.

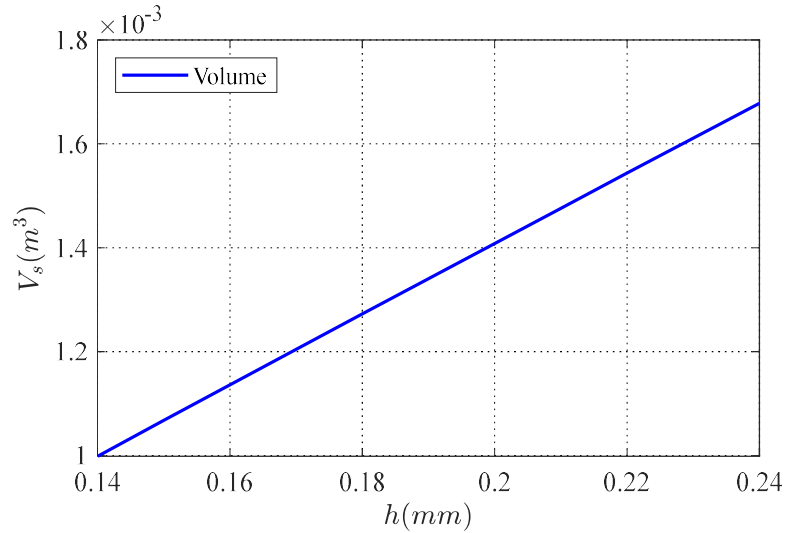


Figure 4.7. The volume of the sleeve air spring at pressure 7 bar.

In this thesis, the mathematical models and simulations were constructed by using MATLAB with Simulink 2020b. In addition, all simulation programs were created by choosing an automatic solver configuration and a sampling time of 0.01 s. The schematic block of the simulation model for the ASVIS is displayed in Figure 4.8. The nonlinear relations which describe spring internal volume and equivalent effective area as an equation of spring height can also be introduced in this block. These relations can be defined both by means of analytic functions and by mapping experimental data, in order to produce curves as shown in Figures 4.4 – 4.7.

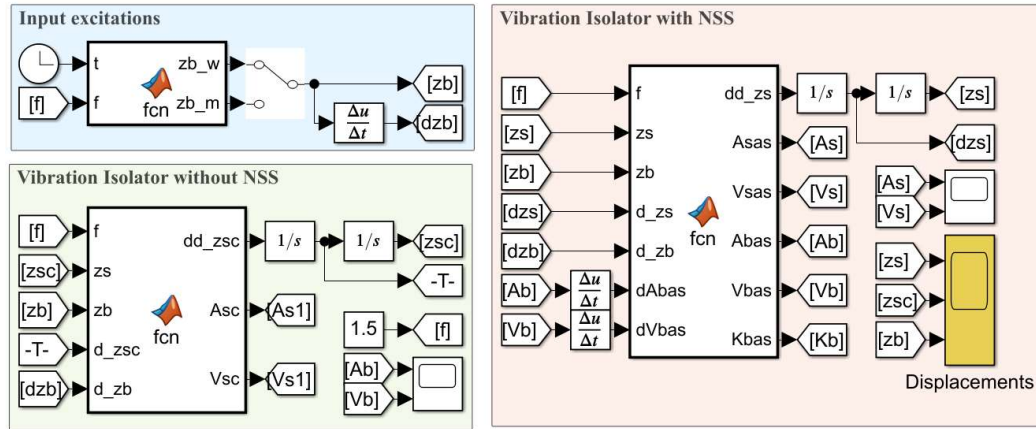


Figure 4.8. Structure of the simulation model for the proposed isolators.

Moreover, the dimension parameters of the ASVIS system in this simulation are presented in Table 4.2. The effective area and volume of air spring as given in Equations (4.4) and (4.5).

Table 4.1. Parameter of the sleeve-type air spring and bellows-type air spring.

Symbol	Value	Unit
n	1.4	-
T	293	K
P_a	1.103×10^5	Pa
P_{se}	3.77×10^5	Pa
P_{be}	3.50×10^5	Pa
L_{se}	200	mm
h_{be}	80	mm

Table 4.2. Dimension parameters of the proposed system in the simulation.

Symbol	Value	Unit
m	150	kg
a	200	mm
b	200	mm
L_b	200	mm
L_h	282.84	mm

4.2.2 ASVIS under Sinusoidal Excitation

The vibration isolation performance of the ASVIS with NSS was analyzed in the presence of sinusoidal excitation. The input excitation was a sinusoid with an amplitude of 20 mm, and the excitation frequency was 1 Hz and 3 Hz.

The displacement responses of the ASVIS with NSS and of the classical air-spring isolator without NSS for sinusoidal wave excitation were compared, as shown in **Figure 4.9**. The solid line, the dashed line, and the dotted line correspond to the ASVIS with NSS, the classical isolator without NSS, and the base excitation, respectively.

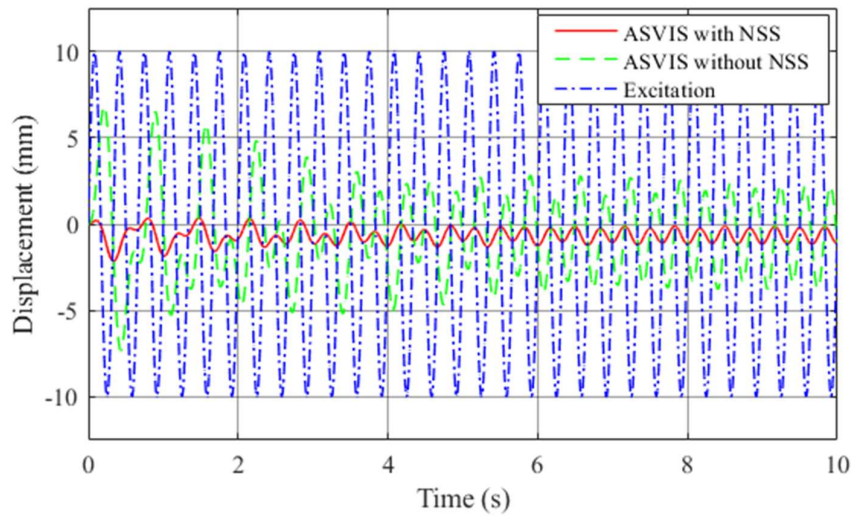


Figure 4.9. Displacement responses of ASVIS for input frequency 3 Hz.

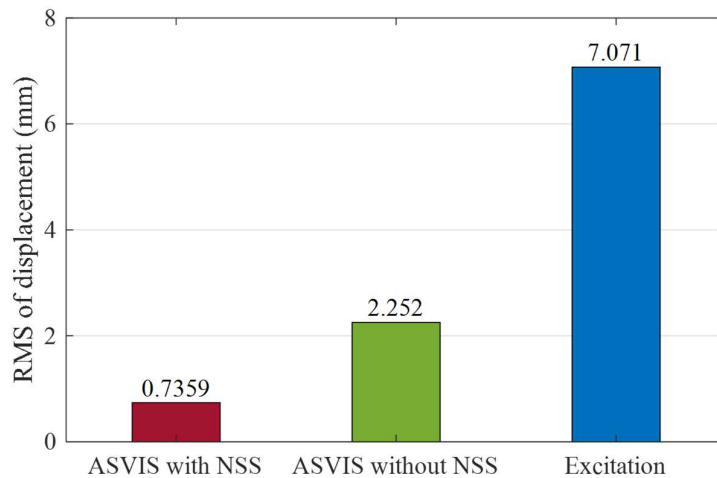


Figure 4.10. RMS value of the displacement.

The simulation results illustrated in **Figure 4.9** showed that the ASVIS with NSS had a higher vibration attenuation rate than the traditional isolator without NSS. The root mean square (RMS) value of the displacement is shown in Figure 4.10. When only a classical isolator

was used, the RMS value of the displacement response decreased by up to 68.15%. After the ASVIS with NSS was applied, the RMS value of the displacement response was significantly reduced by 89.59%.

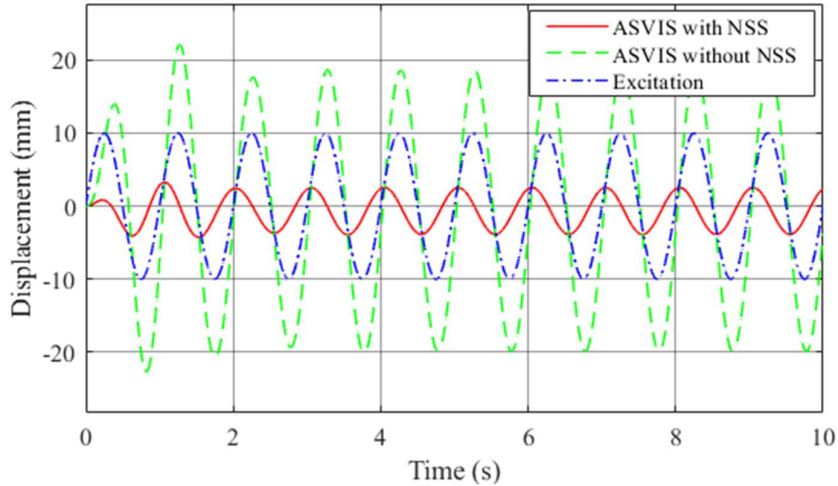


Figure 4.11. Displacement responses of ASVIS for input frequency 1 Hz

Similarly, the excitation frequency of 1 Hz is applied to the ASVIS with NSS and ASVIS without NSS, as shown in Figure 4.11. The results suggested that the displacement of the isolated object using the ASVIS with NSS significantly decreased compared with that at base excitation, whereas the vibration level of the classical isolator without NSS was higher than that at base excitation. Then, the RMS values of the ASVIS with NSS and of the classical isolator without NSS were compared, as shown in Figure 4.12. This figure demonstrates that the RMS values were reduced by 66.65% when using the ASVIS with NSS, whereas, when the same excitation condition was adopted, the RMS values of the displacement response for the classical isolator without NSS increased by 92.62%.

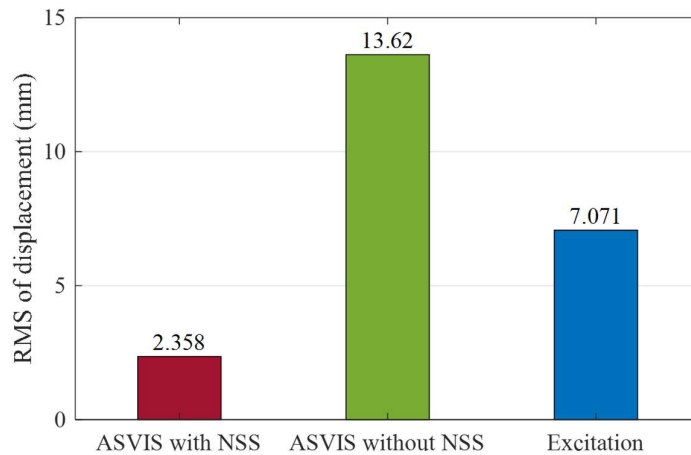


Figure 4.12. RMS value of the displacement for the excitation frequency 1 Hz

4.2.3 ASVIS under Multi-Frequency Wave Excitation

The multi-frequency wave suggested in [11] was employed as the input displacement excitation to evaluate the vibration isolation performance of the ASVIS according to

$$z_b = 5 \sin(1.12\pi t) + 3.5 \sin(3.2\pi t) + 2 \cos(1.8\pi t) + 4 \cos(3.6\pi t) \quad (4.6)$$

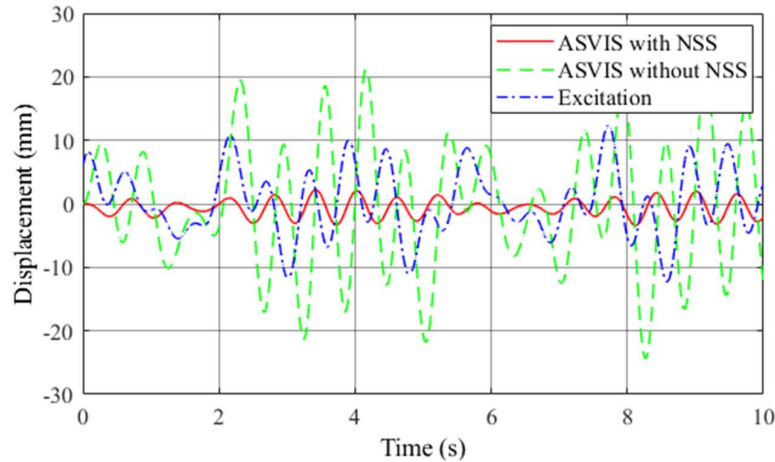


Figure 4.13. Displacement responses of ASVIS under multi-frequency wave excitation.

The displacement response curves in function of the time of the ASVIS with NSS and the classical isolator without NSS were compared, as shown in Figure 4.13. This result illustrates that the ASVIS with NSS performed well in isolating a multi-frequency wave excitation, and the general vibration of the proposed system was remarkably reduced.

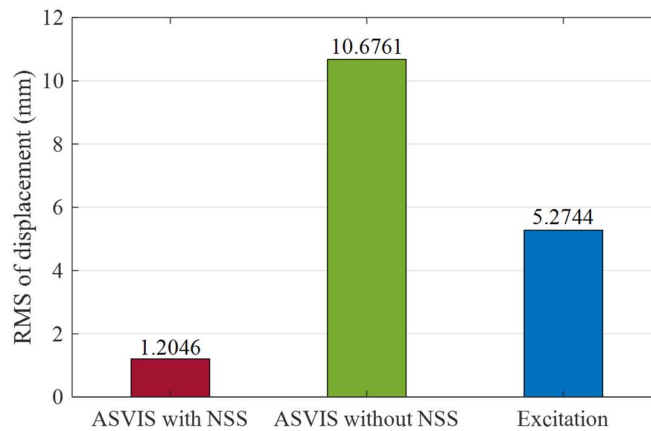


Figure 4.14. RMS value of the displacement

As can be seen from Figure 4.14, the RMS value of the displacement response of the proposed system was significantly lower than the corresponding RMS values of the classical isolator without NSS and of the base excitation. On the contrary, the vibration isolator without NSS decreased the vibration displacement in a high-frequency band, and the vibration peak value after isolation was higher than the amplitude value of the base excitation.

The vibration transmissibility of the ASVIS with NSS and the ASVIS without NSS are compared in Figure 4.15. The proposed model showed a smaller resonance frequency than the ASVIS without the NSS; this was approximately 1.3 Hz for the ASVIS when $P_b = 4$ bar and 1.6 Hz for the ASVIS without NSS. To verify the effects of NSS on the displacement transmissibility of the proposed system, two double convolution bellows of the NSS are pressurized. As a result, the isolation region of the ASVIS with NSS expanded toward low frequencies in comparison that of with the system without NSS. In addition, the ASVIS with NSS showed lower vibration transmissibility than the ASVIS without NSS at the resonance frequency. This result proved that the vibration attenuation of the proposed model was greater than that of the ASVIS without NSS.

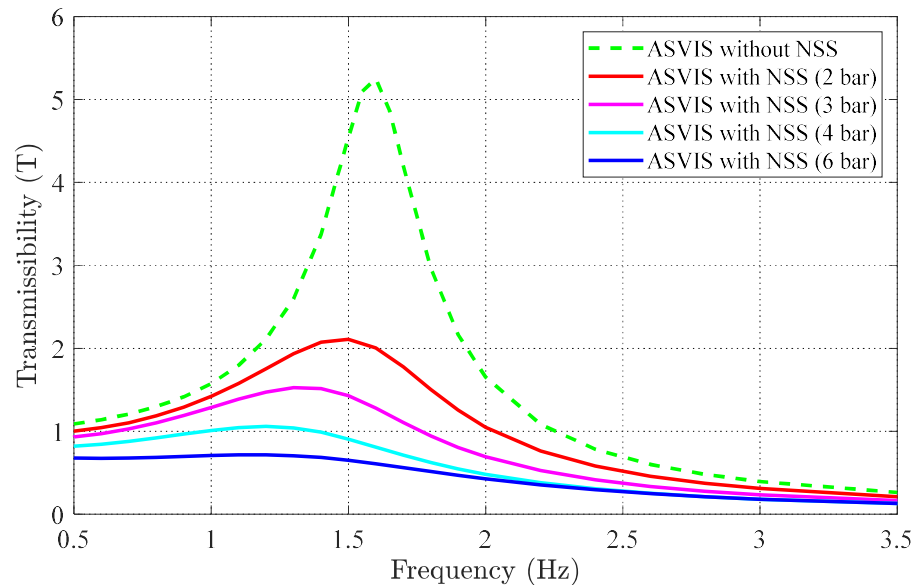


Figure 4.15. Frequency response curves of the ASVIS.

From the above, we can conclude that the classical air-spring isolator without NSS only decreased the vibration displacement at high excitation frequency, while the ASVIS with NSS demonstrated excellent isolation performance at lower excitation frequencies. In particular:

- When the input frequency was lower than the natural frequency of the proposed system, the ASVIS with NSS reduced the excitation amplitude at each frequency component by more than 77.16%. On the contrary, the ASVIS without NSS increased the excitation amplitude to 102.41%.
- When the input frequency was higher than the natural frequency of the proposed system, the displacement response of the classical isolator without NSS decreased by up to 68.15%, while the displacement of the ASVIS with NSS remarkably was reduced by 89.59%.

4.2.4 ASVIS under Random Excitation

For random vibratory excitation, the magnitudes of the displacement, velocity, and acceleration at each moment are unpredictable. However, if the process is repeated under the same conditions, it is possible to forecast a probability that the value of a certain parameter of the process would be within a certain range.

The statistical road profile description specified in ISO 8608 can be used for computer and laboratory road simulations. Standard ISO 8608 specifies the road classification of longitudinal random road profiles based on vertical displacement power spectral density (PSD). The ISO 8608 categorizes the road profiles into eight different classes namely from A to H. Class A is the smoothest road profile with low surface roughness whereas class H represents the worst road case with high surface roughness.

Based on the ISO 8608 norm in [39], the general function of the PSD can be described as bellow

$$G_d(n) = G_d(n_0)(n/n_0)^{-w} \quad (4.7)$$

where $G_d(n)$ is the displacement PSD, n is the spatial frequency, n_0 is the reference spatial frequency, w is the exponent of the PSD. The values of w and $G_d(n_0)$ are specified in **Table 4.3** on basis of the ISO road classification from classes A to H.

Table 4.3. The PSD of the road classification according to the ISO 8608

Road class	The exponent (w)	The $G_d(n_0)$ value of the PSD ($10^{-6} m^3$)		
		Lower limit	Average value	Upper limit
A	2	-	16	32
B	3	32	64	128
C	4	128	256	512
D	5	512	1024	2048
E	6	2048	4094	8192
F	7	8192	16384	32768
G	8	32768	65536	131072
H	9	131072	262144	-
Note: $n_0 = 0.1$ cycles/m, and $w = 2$				

The PSD of random excitation at each frequency n can be represented by an expression of the following form [5]

$$G_d(n) = \lim_{\Delta n \rightarrow 0} \frac{\psi_z^2}{\Delta n} \quad (4.8)$$

where ψ_z^2 is the mean square value of the component of the signal for the frequency n , within the frequency band Δn .

The road profile signal is expressed as a sequence of elevation points uniformly spaced. If the length of the road profile is L and the sampling interval is B , the maximum theoretical sampling spatial frequency is $n_{\max} = 1/B$ and the maximum effective sampling spatial frequency is $n_{\text{eff}} = n_{\max} / 2$ and, within the frequency domain, discretized spatial frequency values n_i are equally spaced with an interval of $\Delta n = 1/L$. The generic spatial frequency value n_i can be regarded as $i\Delta n$ and Equation (4.8) can be written in the discrete form

$$G_d(n_i) = \frac{\psi_z^2(n_i, \Delta n)}{\Delta n} = \frac{\psi_z^2(i\Delta n, \Delta n)}{\Delta n} \quad (4.9)$$

where the value i varying from 0 to $N = n_{\max} / \Delta n = L/B$.

The road profile can be established through a harmonic function according to

$$z_b = Z_i \cos(2\pi n_i d + \varphi) = Z_i \cos(2\pi i \Delta n d + \varphi) \quad (4.10)$$

where Z_i is the amplitude, n_i is the spatial frequency, d is the varies from 0 to L , and φ is the phase angle.

The mean square value of this harmonic signal is expressed as follows

$$\psi_z^2 = \frac{Z_i^2}{2} \quad (4.11)$$

Combing the Equation (4.9), (4.10), and (4.11), we can obtain

$$G_d(n_i) = \frac{\psi_z^2(n_i)}{\Delta n} = \frac{Z_i^2}{2\Delta n} \quad (4.12)$$

Assuming a random phase angle φ_i following a uniform probabilistic distribution within the $0 - 2\pi$ range. The artificial profile can be described as

$$z_b = \sum_{i=0}^N Z_i \cos(2\pi n_i d + \varphi_i) = \sum_{i=0}^N \sqrt{2\Delta n \cdot G_d(i\Delta n)} \cos(2\pi \cdot i \cdot \Delta n \cdot d + \varphi_i) \quad (4.13)$$

Substituting the Equation (4.7) in the Equation (4.13), an random road profile from standard ISO 8608 can be generated by the following equation

$$z_b = \sum_{i=0}^N \sqrt{\Delta n} \cdot 2^w \cdot 10^{-3} \left(\frac{n_0}{i \cdot \Delta n} \right) \cos(2\pi \cdot i \cdot \Delta n \cdot d + \varphi_i) \quad (4.14)$$

For simulation, the roughness profile has been reconstructed by applying the different classes of roads to Equation (4.14) via the application of the Fourier series. The spatial frequency is assumed in the range of 0,011 cycles/m to 2,83 cycles/m. The length of the road classification is equal to 250 m and the speed of the vehicle is assumed 10 m/s. The input values used in the road profile simulation are given in Table 4.4. As in Figure 4.16, the random road profiles of the A to D classes were generated. It is observed that class A is the smoothest road profile with the least amount of surface roughness, while class D is the poorest road profile with the most amount of surface roughness.

Table 4.4. The simulation parameters of the random road profile

Parameter	Value	Unit
n_0	0.1	cycles/m
$G_d(n_0)$	$64 \cdot 10^{-6}$	m^3
w	3	-
v	10	m/s
L	250	m
B	4/36	m
N	2250	-
Δn	1/250	-

To analyze the dynamic response of the ASVIS, road class B is employed as the input random excitation. The displacement response results are displayed in Figure 4.16.

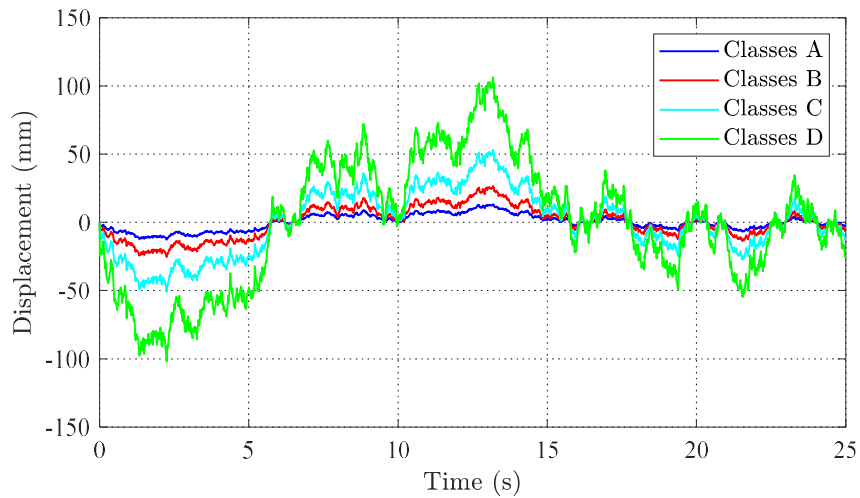


Figure 4.16. Classification of roads

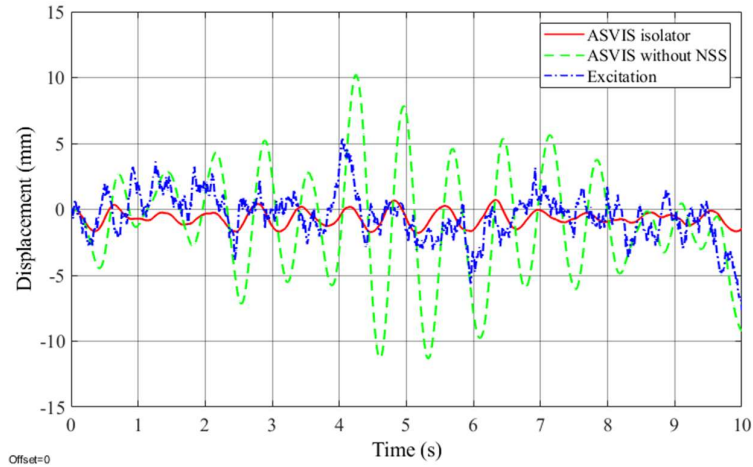


Figure 4.17. Time history results of ASVIS for random excitation.

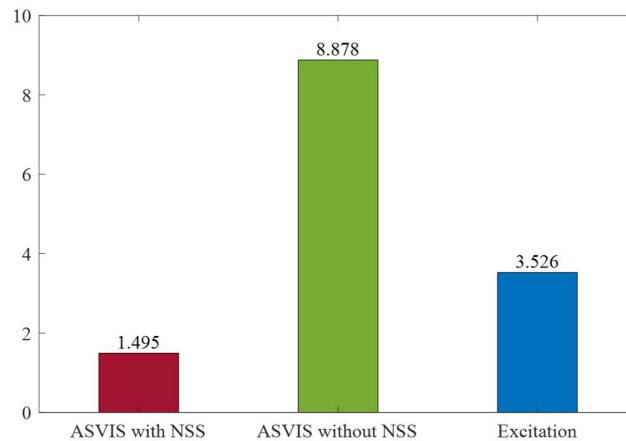


Figure 4.18. RMS value of the displacement

As a results in Figure 4.17, the ASVIS isolator has good performance in isolating a random excitation, and the overall vibration of the system is significantly reduced. The classical vibration isolator only isolates the vibrations in a high-frequency band, but the vibration peak value after isolation even exceeds the maximum value of the excitation. Besides, as shown in Figure 4.18, adding the NSS to the traditional vibration isolation system makes the RMS of the displacement response decrease from 3.52 to 1.49. These demonstrate that the proposed ASVIS vibration isolator can obtain better performance under random excitations.

4.3 Conclusions

From the results above, we can conclude that the proposed ASVIS system maintains excellent vibration isolation performance compared with the classical isolator. Meanwhile, the structure advantage of the convoluted bellows makes it possible to reduce the control difficulty and facilitates the application of ASVIS in the vehicle seats.

Chapter 5

CONTROL SYSTEM MODEL

The advantage of the air-spring system is well-known as clear, cheap, easily maintained, and safe in operation, especially, low stiffness and low damping. But the disadvantage is the high nonlinear properties and difficulty for controlling. In order to solve this disadvantage, some control strategies have been proposed such as C.-M. Lee et al [40] designed a control algorithm for a seat pneumatic suspension with minimum stiffness via the position and velocity data evaluation. Le Thanh Danh et al [12] designed a slider mode control (SMC) for the pneumatic vibration isolation system based on the linearized dynamics. Hyunsup Kim et al [35] developed a sliding mode control algorithm to improve the tracking accuracy of the control and to overcome nonlinearities and uncertainties in the air suspension system. Cong Minh Ho et al [41] proposed an adaptive sliding mode control based on a nonlinear disturbance observer of the pneumatic active suspension to obtain passenger comfort and keep the driving safety.

In general, the air spring system has high nonlinearities due to air compressibility and the airflow through the solenoid valves, and uncertainties are mainly caused by mass variations. Therefore, a control strategy is essential to overcome the nonlinearities and uncertainties and to ensure the driver displacement to track the desired displacement with high accuracy. In addition, the purpose of the controller is to control the air spring to create desired control force to keep the driver at the optimal state under excitation conditions. It means the displacement and acceleration of the driver track references “0”.

In this chapter, we would like to design a sliding mode control for the ASVIS under excitation frequencies of 1 Hz, and all references are treated as “zero”.

5.1 Sliding model control

Generally, based on the Equation (4.1), the state-space form model can be rewritten as

$$\begin{cases} \dot{z}_1 = z_2 \\ \dot{z}_2 = f(x) + g(x)u + d(t) \\ y = z_s \end{cases} \quad (5.1)$$

where $z = [z_1 \ z_2]$, z_1 and z_2 are system states, y is output, $d(t)$ is the external disturbance, and $|d(t)| \leq D_0, |\dot{d}(t)| \leq D$.

$$g(x) = \frac{-A_{sas}}{m}$$

$$f(x) = \frac{P_a A_{sas}}{m} + \left(\frac{2K_b \cos \alpha (z_0 + (b - L_h \cos \alpha) \tan \alpha)}{m \cos \alpha_0} \right) \left(1 - \frac{L_b}{\sqrt{\left(\frac{z_0 + (b - L_h \cos \alpha) \tan \alpha}{2} \right)^2 + L_b^2}} \right)$$

$$\text{with } K_b = (P_b - P_a) \frac{dA_b}{dx} - \frac{n P_b A_b}{V_b} \frac{dV_b}{dx}$$

The SMC is an effective nonlinear control algorithm that has been applied in numerous pneumatic control systems. The design approach of the SMC is composed of two steps. The first step is to design sliding surfaces (s) on which ideal sliding motion can be achieved. The second step is to synthesize a control law so that the trajectories of the closed-loop motion are forced toward the sliding surface. The block diagram of the SMC is presented in Figure 5.1.

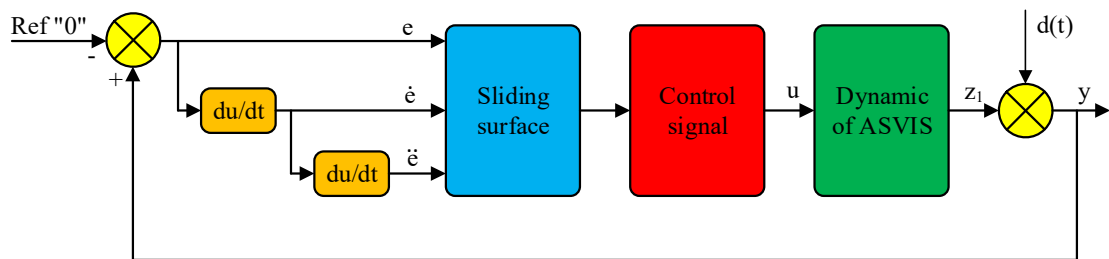


Figure 5.1. Block diagram of sliding mode control

+ Step 1: Design sliding surface

The tracking error of displacement between the reference “0” and the real response z_s of the driver is given by

$$e = y - r \quad (5.2)$$

where r is the setting point of the reference “0”.

Due to the third-order system, the sliding-mode surface is defined as follows

$$s = ce + \dot{e} \quad (5.3)$$

where $c > 0$ is a positive constant.

By substituting Equation (5.2) into (5.3) then taking time derivative of s , the dynamic of s is obtained as follow

$$\dot{s} = c(\dot{y} - \dot{r}) + (\ddot{y} - \ddot{r}) \quad (5.4)$$

Then, via Equation (5.1), above equation is rewritten as follow

$$\dot{s} = f(x) + g(x) + d(t) - \ddot{r} + c\dot{e} \quad (5.5)$$

+ **Step 2:** Design control signal

Sliding-mode control signal consists of two parts, including the equivalent control signal and the switching control signal. The equivalent control signal is the control that keeps the trajectory of the dynamical system on the sliding-mode surface. It can be solved from $\dot{s} = 0$. The switching control signal is to make the trajectory of the dynamical system move toward the sliding-mode surface.

Construct a new dynamic switching function as

$$\sigma = \dot{s} + \lambda s \quad (5.6)$$

where $\lambda > 0$ must be Hurwitz.

When $\sigma = 0$, $\dot{s} + \lambda s = 0$ is asymptotically stable, therefore, $e \rightarrow 0$ and $\dot{e} \rightarrow 0$.

By substituting Equation (5.4) and Equation (5.5) into Equation (5.6), stability analysis is given as follows

$$\sigma = \dot{s} + \lambda s = f(x) + g(x)u + d(t) - \ddot{r} + c\dot{e} + \lambda s \quad (5.7)$$

Sliding-mode control signal is described as

$$u = u_{eq} + u_{sw} \quad (5.8)$$

where u_{eq} and u_{sw} are the equivalent control signal and the switching control signal, respectively.

Letting $\dot{s} = 0$, the equivalent control signal u_{eq} can be expressed as

$$u_{eq} = -\frac{1}{g(x)}(f(x) - \ddot{r} + c\dot{e} + d(t)) \quad (5.9)$$

The switching control signal u_{sw} is designed as

$$u_{sw} = -\frac{1}{g(x)}\eta \text{sgn}(\sigma) \quad (5.10)$$

where η is a positive constant.

Combining Equation (5.9) and Equation (5.10), the control signal u is obtained as

$$u = -\frac{1}{g(x)}(f(x) - \ddot{r} + c\dot{e} + d(t) + \eta \text{sgn}(\sigma)) \quad (5.11)$$

Expanding the function σ by derivative with time, we have

$$\dot{\sigma} = \dot{f}(x) + \dot{g}(x)u + g(x)\dot{u} + \dot{d}(t) - \ddot{r} + c\ddot{e} + \lambda\dot{s} \quad (5.12)$$

Replacing the time derivative of tracking error \ddot{e} from and the time derivative of sliding surface \dot{s} , Equation (5.6) yields

$$\begin{aligned} \dot{\sigma} = & \dot{f}(x) + \dot{g}(x)u + g(x)\dot{u} + \dot{d}(t) - \ddot{r} + c(f(x) + g(x)u + d(t) - \ddot{r}) \\ & + \lambda(f(x) + g(x)u + d(t) - \ddot{r} + c\dot{e}) \end{aligned} \quad (5.13)$$

Expanding Equation (5.13), we can get

$$\begin{aligned} \dot{\sigma} = & \dot{f}(x) - (c + \lambda)\ddot{r} - \ddot{r} + \dot{d}(t) + (c + \lambda)d(t) + (\dot{g}(x) + cg(x) + \lambda g(x))u \\ & + (c + \lambda)f(x) + g(x)\dot{u} + \lambda c\dot{e} \end{aligned} \quad (5.14)$$

Select the dynamic controller as

$$\dot{u} = \frac{1}{g(x)} \begin{pmatrix} -\dot{f}(x) + (c + \lambda)\ddot{r} + \ddot{r} - (\dot{g}(x) + cg(x) + \lambda g(x))u \\ -(c + \lambda)f(x) - \lambda c\dot{e} - \eta \text{sgn}(\sigma) \end{pmatrix} \quad (5.15)$$

From Equations (5.14) and (5.15), we can get

$$\dot{\sigma} = \dot{d}(t) + (c + \lambda)d(t) - \eta \text{sgn}(\sigma) \quad (5.16)$$

Let $\eta > D + (c + \lambda)D_0$, we know

$$\sigma\dot{\sigma} = \sigma(\dot{d}(t) + (c + \lambda)d(t) - \eta \text{sgn}(\sigma)) \quad (5.17)$$

Expanding Equation (5.17), we have

$$\sigma\dot{\sigma} = \sigma(\dot{d}(t) + (c + \lambda)d(t) - \eta|\sigma|) \leq (D + (c + \lambda)D_0)\sigma - \eta|\sigma| < 0 \quad (5.18)$$

Therefore, according to the Lyapunov stability theory, for the nonlinear dynamical ASVIS system described by Equation (5.1), under the control law (5.11), the closed-loop control system of ASVIS is stable.

5.2 Simulation results with SMC

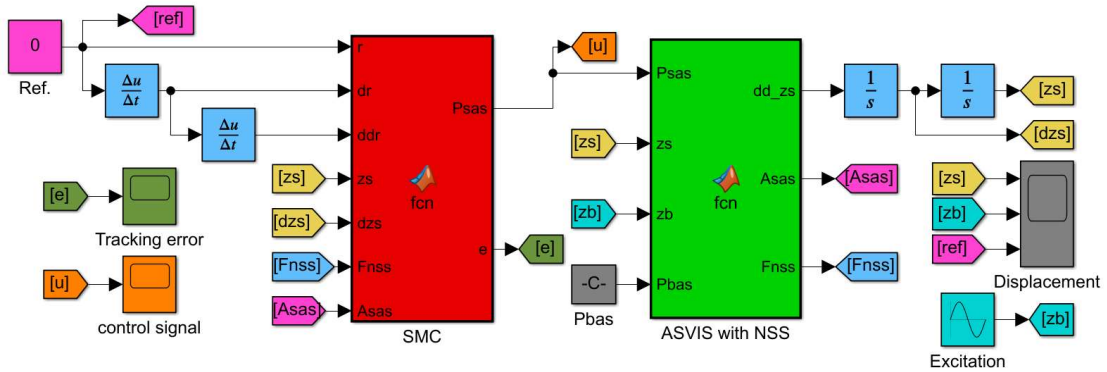


Figure 5.2. Block diagram of the SMC in the Simulink environment.

The control algorithm is designed in the MATLAB/Simulink environment 2020. Figure 5.2 displays the overall control scheme of the ASVIS system using the sliding mode controller.

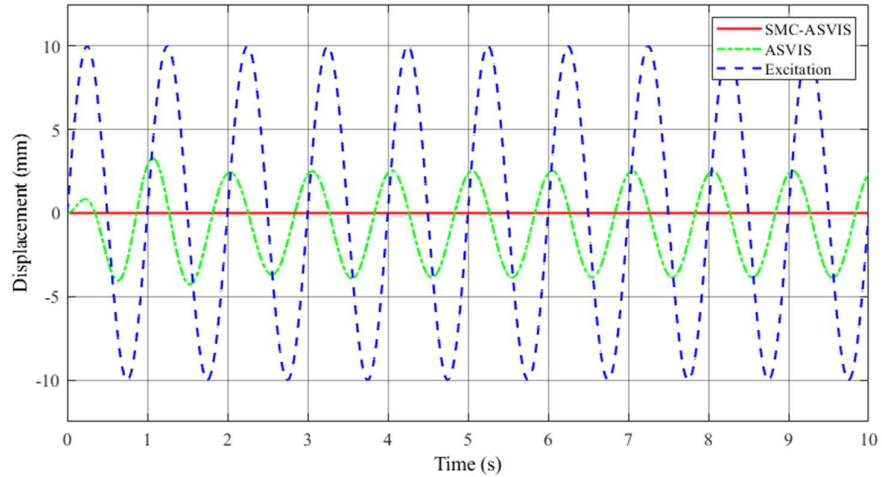


Figure 5.3. Response of the displacement

When the base is excited by a sinusoidal wave with an amplitude of 40 mm and a frequency of 1.0 Hz, the displacement response of the driver seat is presented in Figure 5.3. The dashed line exhibits the excitation signal, the solid line is used to denote the displacement response controlled by the SMC controller. As a results, the displacement response of the vehicle seat is kept in an optimal state under excitation conditions on the road. This concludes that the active system with NSS suppresses the vibrations from the base more effectively than the active system without a controller.

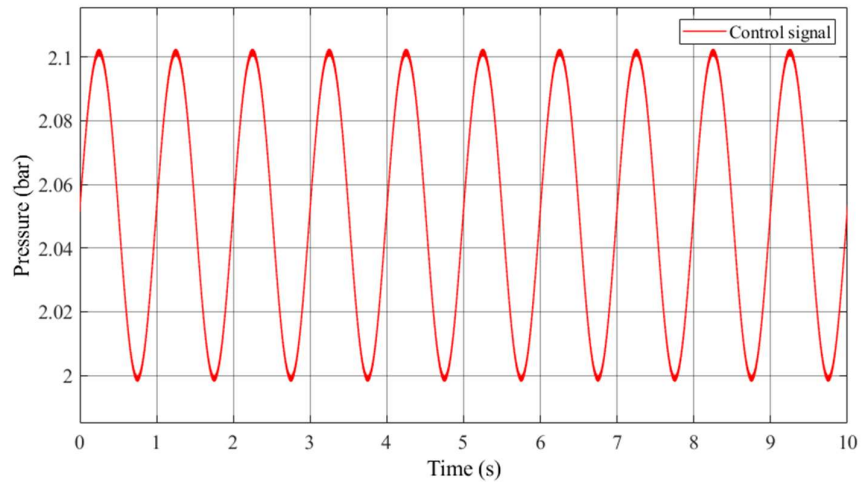


Figure 5.4. Control signal

Figure 5.4 and Figure 5.5 show the control signal and tracking error of the SMC controller, respectively. It can be seen that the proposed SMC controller is suitable to control the vibratory isolation of the active system using NSS. However, the chattering phenomenon on the conventional sliding mode control has not been removed completely.

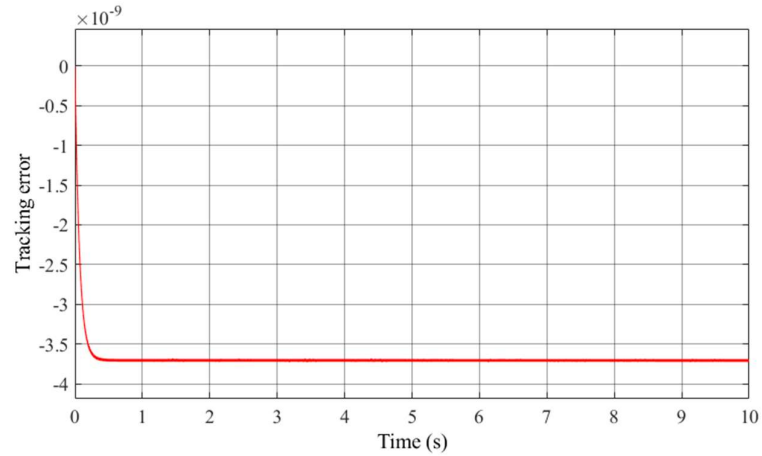


Figure 5.5. Tracking error

5.3 Conclusions

This chapter designed an SMC controller for the AVIS to improve the isolation performance. First, an SMC controller was designed and successfully employed for the proposed system. Then, the stability of the controllers is analyzed in sense of the Lyapunov stability theorem. The resulting performances of the ASVIS system with an SMC controller are far better than the passive isolator without control.

CONCLUSION AND FUTURE WORK

6.1 Summary

A vehicle seat should ideally have a high static stiffness to withstand high loads without causing excessive displacement, and a low dynamic stiffness to keep the natural frequency of the system as low as possible in order to isolate low-frequency excitation. This problem was overcome by proposing a vibration isolation model based on a negative stiffness structure. Due to the opposite of the negative stiffness element and the positive stiffness element, the ASVIS has a low nonlinear stiffness but maintains a high static stiffness. As result, the proposed system reduces vibration in the low excitation frequency region while ensuring load-bearing capacity.

This study introduced the ASVIS system with a negative-stiffness structure, which was designed to improve the driver's safety and health in low excitation frequencies. The ASVIS system is included two double-convoluted bellows elements in the horizontal direction and a sleeve-type air spring element in the vertical direction. The proposed system was demonstrated to produce increased static stiffness and reduced dynamic stiffness, thus maximizing the comfort of the driver.

Compared with the traditional vibration isolation system, the ASVIS system employing air springs has certain advantages as described below:

- + Compared with the mechanical spring system, the spring rate of system with air spring is low to provide the soft and comfortable ride.

- + Variable load carrying capability: The load an air spring carries can be adjusted over a wide range simply by changing the air pressure while keeping the air spring's static height the same. Whereas the mechanical linear springs do not have that wide range of load carrying capacity.

- + Adjustable spring stiffness: For air springs, the spring stiffness could be adjusted by changing the air pressure while keeping the air spring height. For the classical system with mechanical spring, the spring stiffness is always a constant value.

- + User friendly height control: An air spring's desired height can be modulated by connecting the air spring to a compressed air source whereas the desired static height for mechanical spring changes with the load and cannot be modulated.

+ Quiet operation: Since the flexible rubber member of the air spring moves freely, there is not much noise coming from the pneumatic suspension system. For the classical system with mechanical spring, noisy operation could result due to contact between mechanical parts.

Moreover, the simulation was realized to evaluate the isolation performance of the proposed system. Where, the different excitation signals are considered including sinusoidal waves, multi-frequency waves, and random excitations. In addition, the comparison with the classical isolator without NSS was mentioned. Based on the obtained results, we can conclude that the proposed ASVIS with NSS provides excellent vibration isolation performance in comparison with the classical isolator without NSS. Furthermore, the air spring structure has the advantage of reducing calculation difficulty when ASVIS is used in complex vibration isolation structures.

Finally, via the SMC control method designed, the isolation performance of the ASVIS system was assessed under the sinusoidal excitation condition. The resulting performances of the ASVIS system are far better than the passive isolator without NSS.

6.2 Future work

In this study, the generated force of the double convolution bellows directly affected the desired control force of the ASVIS system. In the future, another control strategy that can be investigated is the negative stiffness control via controlling the convoluted bellows.

In addition, the chattering phenomenon on the conventional sliding mode control has not been removed completely. Thus, future research may concentrate on the adaptive SMC of the air-spring pressure in order to achieve zero dynamic stiffness over a larger range of displacements.

In the ASVIS, the friction of air spring effect of both air springs was ignored. Nonetheless, in practice, this phenomenon still exists and has an impact on the vibration isolation performance of the system. In the future, the effect of the friction phenomenon on the characteristic of the vibration transmissibility of the ASVIS should be investigated.

References

- [1] M. J. Griffin, "Preface," in *Handbook of Human Vibration*, M. J. Griffin Ed. London: Academic Press, 1990, pp. v-vii.
- [2] N. J. E. Mansfield, "Human Response to Vibration (1st ed.). CRC Press.," 2004, doi: <https://doi.org/10.1201/b12481>.
- [3] G. S. Paddan and M. J. Griffin, "Evaluation of Whole-Body Vibration in Vehicles," *Journal of Sound and Vibration*, vol. 253, no. 1, pp. 195-213, 2002, doi: <https://doi.org/10.1006/jsvi.2001.4256>.
- [4] X. Jin *et al.*, "Effects of Sinusoidal Whole Body Vibration Frequency on Drivers' Muscle Responses," 2015. [Online]. Available: <https://doi.org/10.4271/2015-01-1396>.
- [5] Rivin, EI , Author, "Passive Vibration Isolation," *Applied Mechanics Reviews*, vol. 57, no. 6, pp. B31-B32, 2005, doi: 10.1115/1.1849173.
- [6] J. Yang, "Force transmissibility and vibration power flow behaviour of inerter-based vibration isolators," *Journal of Physics: Conference Series*, vol. 744, p. 012234, 2016/09 2016, doi: 10.1088/1742-6596/744/1/012234.
- [7] J. Yang, J. Z. Jiang, X. Zhu, and H. Chen, "Performance of a dual-stage inerter-based vibration isolator," *Procedia Engineering*, vol. 199, pp. 1822-1827, 2017/01/01/ 2017, doi: <https://doi.org/10.1016/j.proeng.2017.09.097>.
- [8] I. A. Karnovsky and E. Lebed, *Theory of Vibration Protection*. Springer Cham, 2016, pp. XLV, 674.
- [9] P. M. Alabuzhev and E. I. Rivin, *Vibration Protection And Measuring Systems With Quasi-Zero Stiffness*. Taylor & Francis, 1989.
- [10] D. Platus, *Negative-stiffness-mechanism vibration isolation systems* (SPIE Technical: OPTCON '91). SPIE, 1992.
- [11] T. D. Le and K. K. Ahn, "A vibration isolation system in low frequency excitation region using negative stiffness structure for vehicle seat," (in English), *Journal of Sound and Vibration*, vol. 330, no. 26, pp. 6311-6335, Dec 19 2011, doi: 10.1016/j.jsv.2011.07.039.
- [12] L. T. Danh and K. K. Ahn, "Active pneumatic vibration isolation system using negative stiffness structures for a vehicle seat," (in English), *Journal of Sound and Vibration*, vol. 333, no. 5, pp. 1245-1268, Feb 28 2014, doi: 10.1016/j.jsv.2013.10.027.
- [13] J. Yang, Y. P. Xiong, and J. T. Xing, "Dynamics and power flow behaviour of a nonlinear vibration isolation system with a negative stiffness mechanism," *Journal of Sound and Vibration*, vol. 332, no. 1, pp. 167-183, 2013/01/07/ 2013, doi: <https://doi.org/10.1016/j.jsv.2012.08.010>.
- [14] B. Shi, J. Yang, and T. Li, "Enhancing Vibration Isolation Performance by Exploiting Novel Spring-Bar Mechanism," *Applied Sciences*, vol. 11, no. 19, 2021, doi: 10.3390/app11198852.
- [15] M. Sun, Z. Dong, G. Song, X. Sun, and W. Liu, "A Vibration Isolation System Using the Negative Stiffness Corrector Formed by Cam-Roller Mechanisms with Quadratic Polynomial Trajectory," *Applied Sciences*, vol. 10, no. 10, 2020, doi: 10.3390/app10103573.
- [16] Y. Yao, H. Li, Y. Li, and X. Wang, "Analytical and experimental investigation of a high-static-low-dynamic stiffness isolator with cam-roller-spring mechanism," *International Journal of Mechanical Sciences*, vol. 186, 2020, doi: 10.1016/j.ijmecsci.2020.105888.

- [17] Y. Zheng, X. Zhang, Y. Luo, B. Yan, and C. Ma, "Design and experiment of a high-static–low-dynamic stiffness isolator using a negative stiffness magnetic spring," *Journal of Sound and Vibration*, vol. 360, pp. 31-52, 2016, doi: 10.1016/j.jsv.2015.09.019.
- [18] E. Palomares, A. J. Nieto, A. L. Morales, J. M. Chicharro, and P. Pintado, "Numerical and experimental analysis of a vibration isolator equipped with a negative stiffness system," *Journal of Sound and Vibration*, vol. 414, pp. 31-42, 2018, doi: 10.1016/j.jsv.2017.11.006.
- [19] A. Carrella, M. J. Brennan, and T. P. Waters, "Static analysis of a passive vibration isolator with quasi-zero-stiffness characteristic," *Journal of Sound and Vibration*, vol. 301, no. 3-5, pp. 678-689, 2007, doi: 10.1016/j.jsv.2006.10.011.
- [20] C.-C. Lan, S.-A. Yang, and Y.-S. Wu, "Design and experiment of a compact quasi-zero-stiffness isolator capable of a wide range of loads," *Journal of Sound and Vibration*, vol. 333, no. 20, pp. 4843-4858, 2014/09/29/ 2014, doi: <https://doi.org/10.1016/j.jsv.2014.05.009>.
- [21] Y. Chang, J. Zhou, K. Wang, and D. Xu, "A quasi-zero-stiffness dynamic vibration absorber," *Journal of Sound and Vibration*, vol. 494, 2021, doi: 10.1016/j.jsv.2020.115859.
- [22] C. Liu and K. Yu, "Accurate modeling and analysis of a typical nonlinear vibration isolator with quasi-zero stiffness," *Nonlinear Dynamics*, vol. 100, no. 3, pp. 2141-2165, 2020, doi: 10.1007/s11071-020-05642-2.
- [23] J. Yang, J. Z. Jiang, and S. A. Neild, "Dynamic analysis and performance evaluation of nonlinear inerter-based vibration isolators," *Nonlinear Dynamics*, vol. 99, no. 3, pp. 1823-1839, 2019, doi: 10.1007/s11071-019-05391-x.
- [24] J. Zhou, X. Wang, D. Xu, and S. Bishop, "Nonlinear dynamic characteristics of a quasi-zero stiffness vibration isolator with cam–roller–spring mechanisms," *Journal of Sound and Vibration*, vol. 346, pp. 53-69, 2015, doi: 10.1016/j.jsv.2015.02.005.
- [25] K. Ye, J. C. Ji, and T. Brown, "Design of a quasi-zero stiffness isolation system for supporting different loads," *Journal of Sound and Vibration*, vol. 471, 2020, doi: 10.1016/j.jsv.2020.115198.
- [26] S. Yuan *et al.*, "A tunable quasi-zero stiffness isolator based on a linear electromagnetic spring," *Journal of Sound and Vibration*, vol. 482, 2020, doi: 10.1016/j.jsv.2020.115449.
- [27] X. Sun, X. Jing, J. Xu, and L. Cheng, "Vibration isolation via a scissor-like structured platform," *Journal of Sound and Vibration*, vol. 333, no. 9, pp. 2404-2420, 2014/04/28/ 2014, doi: <https://doi.org/10.1016/j.jsv.2013.12.025>.
- [28] M. Sun, G. Song, Y. Li, and Z. Huang, "Effect of negative stiffness mechanism in a vibration isolator with asymmetric and high-static-low-dynamic stiffness," *Mechanical Systems and Signal Processing*, vol. 124, pp. 388-407, 2019/06/01/ 2019, doi: <https://doi.org/10.1016/j.ymssp.2019.01.042>.
- [29] C. Wei, K. Zhang, C. Hu, Y. Wang, H. Taghavifar, and X. Jing, "A tunable nonlinear vibrational energy harvesting system with scissor-like structure," *Mechanical Systems and Signal Processing*, vol. 125, pp. 202-214, 2019, doi: 10.1016/j.ymssp.2018.06.007.
- [30] G. Quaglia and M. Sorli, "Air Suspension Dimensionless Analysis and Design Procedure," *Vehicle System Dynamics*, vol. 35, no. 6, pp. 443-475, 2001, doi: 10.1076/vesd.35.6.443.2040.
- [31] C. M. Lee, V. N. Goverdovskiy, and A. I. Temnikov, "Design of springs with “negative” stiffness to improve vehicle driver vibration isolation," *Journal of Sound and Vibration*,

- vol. 302, no. 4, pp. 865-874, 2007/05/22/ 2007, doi: <https://doi.org/10.1016/j.jsv.2006.12.024>.
- [32] E. Palomares, A. L. Morales, A. J. Nieto, J. M. Chicharro, and P. Pintado, "Improvement of Comfort in Suspension Seats with a Pneumatic Negative Stiffness System," *Actuators*, vol. 9, no. 4, 2020, doi: 10.3390/act9040126.
- [33] Firestone, "Engineering Manual & Design Guide," 2020. [Online]. Available: <https://firestoneip.com>.
- [34] Z. Qi, F. Li, and D. Yu, "A three-dimensional coupled dynamics model of the air spring of a high-speed electric multiple unit train," *Proceedings of the Institution of Mechanical Engineers, Part F: Journal of Rail and Rapid Transit*, vol. 231, no. 1, pp. 3-18, 2016, doi: 10.1177/0954409715620534.
- [35] K. Hyunsup and L. Hyeongcheol, "Height and Leveling Control of Automotive Air Suspension System Using Sliding Mode Approach," *IEEE Transactions on Vehicular Technology*, vol. 60, no. 5, pp. 2027-2041, 2011, doi: 10.1109/tvt.2011.2138730.
- [36] J.-J. Chen, Z.-H. Yin, S. Rakheja, J.-H. He, and K.-H. Guo, "Theoretical modelling and experimental analysis of the vertical stiffness of a convoluted air spring including the effect of the stiffness of the bellows," *Proceedings of the Institution of Mechanical Engineers, Part D: Journal of Automobile Engineering*, vol. 232, no. 4, pp. 547-561, 2017, doi: 10.1177/0954407017704589.
- [37] M. Krack and J. Gross, *Harmonic Balance for Nonlinear Vibration Problems*. 2019.
- [38] P. Beater, *Pneumatic Drives*. Springer Berlin, Heidelberg, 2007.
- [39] I. O. f. Standardization, *ISO 8608 : Mechanical Vibration, Road Surface Profiles, Reporting of Measured Data: International Standard*. International Organization for Standardization, ISO, 2016.
- [40] C. M. Lee, A. H. Bogatchenkov, V. N. Goverdovskiy, Y. V. Shynkarenko, and A. I. Temnikov, "Position control of seat suspension with minimum stiffness," *Journal of Sound and Vibration*, vol. 292, no. 1-2, pp. 435-442, 2006, doi: 10.1016/j.jsv.2005.08.027.
- [41] C. M. Ho, D. T. Tran, and K. K. Ahn, "Adaptive sliding mode control based nonlinear disturbance observer for active suspension with pneumatic spring," *Journal of Sound and Vibration*, vol. 509, 2021, doi: 10.1016/j.jsv.2021.116241.

Publications

A. International Journals

[1] Nguyen CH, Ho CM, Ahn KK. An Air Spring Vibration Isolator Based on a Negative-Stiffness Structure for Vehicle Seat. *Applied Sciences*. 2021; 11(23):11539. <https://doi.org/10.3390/app112311539>.

[2] C. M. Ho, D. T. Tran, C. H. Nguyen and K. K. Ahn, "Adaptive Neural Command Filtered Control for Pneumatic Active Suspension with Prescribed Performance and Input Saturation," in *IEEE Access*, vol. 9, pp. 56855-56868, 2021, DOI: 10.1109/ACCESS.2021.3071322.

[3] Ho CM, Nguyen CH, Ahn KK. Adaptive Fuzzy Observer Control for Half-Car Active Suspension Systems with Prescribed Performance and Actuator Fault. *Electronics*. 2022; 11(11):1733. <https://doi.org/10.3390/electronics11111733>.

B. International Conference Papers

[1] C. H. Nguyen, C. M. Ho and K. K. Ahn, "Numerical Analysis of Vibration Isolator Using Negative Stiffness Mechanism for Vehicle Seats," 2021 24th International Conference on Mechatronics Technology (ICMT), 2021, pp. 1-6, doi: 10.1109/ICMT53429.2021.9687145.

Appendix

I. Technical data of Sleeve Air Spring

- Model: **W02-358-7012**
- Technical data

Style number	Design height (mm)	Load at design height (kN)			Natural frequency at 7 Bar (Hz)	% of isolation at forced frequency		
		3 Bar	5 Bar	7 Bar		7 Hz	13 Hz	25 Hz
7012	216	1.7	3.2	4.5	1.6	93.9	98.5	99.6

- The constant pressure characteristics of the Sleeve air spring

Force table							
Assembly Height (mm)	Volume at 7 Bar (cu cm)	Eff. Area at 7 Bar (cu sq)	kN Force				
			3 Bar	4 Bar	5 Bar	6 Bar	7 Bar
240	1676	56	1.83	2.45	3.06	3.52	3.94
220	1547	62	1.82	2.52	3.18	3.81	4.37
200	1409	65	1.77	2.48	3.15	3.89	4.56
180	1271	65	1.71	2.42	3.07	3.83	4.51
160	1134	61	1.65	2.33	2.97	3.67	4.30
140	1000	58	1.63	2.22	2.83	3.48	4.06

- Dynamic Characteristics of the Sleeve air spring

Dynamic characteristics at 215 mm design height			
Gauge pressure (Bar)	Load (kN)	Spring rate (kN/m)	Natural frequency (Hz)
3	1.81	13	1.31
4	2.51	18	1.33
5	3.18	23	1.33
6	3.85	33	1.47
7	4.44	43	1.55

- Assembly weight: 0.82 kg.

II. Technical data of Double Convoluted Bellows

- Model: **EB-80-45**
- Product range overview

Function	Single-acting
Type	Double-bellows actuator
Size	80
Stroke [mm]	45
Thrust [kN]	1.4
Recommended operating height [mm]	90

- General technical data

Size	80
Pneumatic port	G1/4
Stroke	
Single-bellows actuator [mm]	20
Double-bellows actuator [mm]	45
Model of operation	Single-acting
Type of mounting	Via internal thread
Mounting position	Any

- Operating and environmental conditions

Size	80
Operating medium	Compressed air to ISO 8573-1:2010 [-:-:4]
Note on the operating/control medium1)	Lubricated operation not possible
Operating pressure [bar]	0 ... 8
Ambient temperature [°C]	-40 ... +70
Corrosion resistance class CRC	0

- Weight

Size	80
Single-bellows actuator	500 [g]
Double-bellows actuator	500 [g]